MAP-0/660
For Author's Correction Only

Meteorol Atmos Phys 000, 1–21 (2004)
DOI 10.1007/s00703-004-0079-6

Meteorology and Atmospheric Physics
Printed in Austria

[1] Department of Marine, Earth, and Atmospheric Sciences, North Carolina State University, Raleigh, NC
[2] MESO Inc., Raleigh, NC
[3] USDA/Forest Service, North Central Research Station, East Lansing, MI

Characterizing the severe turbulence environments associated with commercial aviation accidents. Part 2: Hydrostatic mesoscale numerical simulations of supergradient wind flow and streamwise ageostrophic frontogenesis

M. L. Kaplan[1], A. W. Huffman[1], K. M. Lux[1], J. D. Cetola[1], J. J. Charney[3], A. J. Riordan[1], Y.-L. Lin[1], and **K. T. Waight III[2]**

With 17 Figures

Received April ●, 2003; revised October 1, 2003; accepted January 22, 2004
Published online: ● ● ●

Summary

Simulation experiments reveal key processes that organize a hydrostatic environment conducive to severe turbulence. The paradigm requires the juxtaposition of the entrance region of a curved jet streak, which is highly subgeostrophic, with the entrance region of a straight jet streak, which is highly supergeostrophic. The wind and mass fields become misphased as the entrance regions converge, resulting in significant spatial variation of inertial forcing, centripetal forcing, as well as along and cross-stream pressure gradient forcing over a meso-β scale region. Maxima of these forces are misphased where the two dissimilar jet streaks converge and geostrophic balance is disrupted. Velocity divergence within the subgeostrophic region of largest upstream-directed pressure gradient force and velocity convergence near the region of largest downstream-directed centripetal/inertial-advective forcing act to produce a mesoscale front due to spatially varying confluent flow flanked by zones of increasing velocity divergence. This results in frontogenesis as well as the along-stream divergence of cyclonic and convergence of cyclonic ageostrophic vertical vorticity. The nonuniform centripetally forced mesoscale front becomes the locus of large gradients of ageostrophic vertical vorticity along an overturning isentrope. This region becomes favorable for streamwise vorticity gradient formation enhancing the environment for the organization of horizontal vortex tubes in the presence of buoyant forcing. This is because the mesoscale convergence of vertical vorticity on an overturning isentropic surface creates vertical rotation for the development of horizontal vorticity in regions where isentropic surfaces overturn. Vorticity, shear, and buoyancy are focused in one location by this front thus favoring an environment favorable for microvortex formation leading to turbulence.

1. Introduction

Atmospheric turbulence has long represented one of the most demanding conceptual and forecasting challenges in meteorology. The fine spatial and temporal scale of turbulence and the coarse nature of atmospheric observations make even mapping the occurrence of turbulence, let alone forecasting it, extraordinarily difficult. Jet stream entrance regions have been known for many years to be preferred regions for turbulence (e.g., Reiter and Nania, 1964; Mancuso and

Endlich, 1966; Roach, 1970; Reed and Hardy, 1972; Shapiro, 1976; Gidel and Shapiro, 1979; Kennedy and Shapiro, 1980; Uccellini et al, 1986; Keller, 1990; Ellrod and Knapp, 1992). In Kaplan et al (2003) this finding was reconfirmed in a 44-case study synoptic observational analysis of accident-producing turbulence. However, the dynamical processes which make jet entrance regions favored zones for severe turbulence are not well understood. Therefore, severe turbulence is not always accurately anticipated in advance as many well-organized jet entrance regions are largely devoid of even light turbulence while others produce extremely severe turbulence.

Previous studies (e.g., Uccellini et al, 1986; Keller, 1990; Marroquin, 1998) found that air parcels arriving from different regions in vertically sheared flows produce locally low Richardson number or Richardson number tendency. Hence, they produce a region of significant turbulence probability in evolving frontal zones in confluent jet stream entrance regions. Frontal zones and Richardson number variability are coupled because frontal zones are regions of deformed and, therefore, overturned isentropes, hence, they are regions of low static stability and significant vertical wind shears that result in reduced Richardson number values. Low Richardson number and/or Richardson number tendency indicates that the greatest wind shear and buoyancy potential for turbulence kinetic energy generation exists in frontal zones accompanying jet entrance regions. However, forecasting indices, which typically rely solely on these Richardson number-based fields, are rarely employed operationally. These indices alone are not always successful at discriminating between turbulent and nonturbulent regimes because of the very fine scale structure of the frontal zones that organize the turbulent event. The organizing circulation is so fine scale that only the environment that produces it can be sensed or simulated. Rarely can turbulence itself be accurately forecasted operationally without the inclusion of kinematic forcing, e.g., velocity deformation, potential vorticity, and/or velocity divergence (e.g., Ellrod and Knapp, 1992; Sharman et al, 2000). As an example, a useful index employed by the National Weather Service is the Ellrod and Knapp index, which is simply the product of the deformation and the vertical wind shear. The ITFA index, operationally employed at the National Center for Atmospheric Research, is a synthesis of many fields, which are explicit functions of both Richardson number and flow kinematics. Hence, given that both unique kinematic as well as vertical wind shear and buoyancy forcing are diagnosed in regions of turbulence, there can be a great deal of uncertainty concerning what processes accompanying jet entrance regions consistently organize the environment that creates turbulence of greater than moderate intensity. Adding to the theoretical complexity, Knox (1997) noted how inertial instability and geostrophic adjustment are likely maximized in many case studies where clear air turbulence may occur. Since inertial instability can be directly related to low potential vorticity and low Richardson number, which are typical of anticyclonically-shearing jet streams embedded within strong frontal systems, it represents yet another possible mechanism of turbulence development generally related to jet entrance regions, fronts, low Richardson numbers, deformation, and vorticity (Stone, 1966). Thus, buoyancy-based forcing, shear-based forcing, kinematics-based forcing, and complex combinations thereof can be related to characterizing the environment that organizes turbulence but may or may not be a discriminating condition for the development of severe accident-producing turbulence. This issue of unambiguously discriminating when and where an environment will organize fine scale severe turbulence represents an unsolved problem in applied meteorology.

Recently, Andreassen et al (1998) presented idealized numerical simulation results and Clark et al (2000) presented real data numerical simulations, as well as observationally-derived evidence, of vortex tubes in the vicinity of severe turbulence. Both groups hypothesize the possible mutual interaction of vortex tubes at the meso and microscale as key mechanisms in the organization of severe clear air and terrain-induced turbulence. Regions of strong vertical vorticity at the mesoscale often produce microscale maxima of horizontal vorticity due to flow blocking and/or convergence near terrain or due to local solenoidal forcing (e.g., Clark et al, 2000). Both sets of numerical simulations unambiguously indicate that a downscale nonlinear amplification

of waves and vortices can focus significant rotation (vortex tubes) into a highly specific region, which could, in theory, produce a region of well-mixed and rotating flow causing extreme turbulence in the path of an aircraft. This is facilitated where convergence and vorticity phase within certain types of frontal zones. This is most likely to occur if one observes a very intense vertical transport of rotation in the form of vortices, i.e., if wave breaking transports momentum vertically as vorticity is converged into local regions. However, it has never been unambiguously and conclusively proven that vortices cause the type of turbulence that results in aviation accidents, though a case was made for such by Parks et al (1994). Nevertheless, Clark et al (2000) provided unambiguous evidence that observed turbulence and vortex tube generation was collocated for a case of mountain turbulence.

There are two fundamental questions to be addressed. Are clear air and convective turbulence, which often occur upstream or downstream from mountains, the result of intense vortex tube formation? How do they evolve within favored locations accompanying jet stream entrance regions where strong 3-dimensional wind shears, low buoyancy, and large values of potential vorticity exist, but where no fixed blocking mechanism is in place? Clearly, there is a need for a coherently crafted multi-scale theory/paradigm based on several real-data observational analyses and multi-scale numerical simulations. This could offer improved understanding of how preferred zones for severe turbulence are organized in both convective and clear air environments. If such a paradigm could be developed, the result would be the formulation of an algorithm, which could be employed in turbulence forecasting that represents a potential improvement to the state of the science. It is the goal of this paper to build on the findings presented in Kaplan et al (2003) by synthesizing such an original coherent original paradigm at the hydrostatic subsynoptic scales of motion whose end product is to improve the accuracy with which accident-producing turbulence is predicted in both convective and clear air environments. The organization of streamwise gradients of ageostrophic relative vorticity in the preturbulent environment is key to this paradigm. This is so because the convergence of the rotation at the mesoscale affects the development of microscale vortices as indicated by vorticity source terms in the horizontal vorticity equations. This is facilitated by very strong inertial-advective forcing accompanying streamwise gradients of vertical vorticity in the presence of confluent flow. In subsequent papers we will, first, demonstrate the theory supporting a transition from a hydrostatic to a nonhydrostatic sequence of processes that organizes an environment favorable for horizontal vortex tube formation from streamwise gradients of hydrostatic ageostrophic relative vorticity. Second, we will endeavor to demonstrate the real-time operational application of an index, based on this theory, for a wide variety of moderate to severe mountain, clear air, and, primarily, convective turbulence case studies.

In this paper we will utilize meso-α and meso-β scale hydrostatic numerical simulations of recurring multi-scale dynamical processes that result in accident-producing turbulence. The focus will be on turbulence in proximity to deep moist convection; however, a clear air turbulence (CAT) case study is also examined in an effort to show how the hydrostatic precursor environment for both severe CAT and convectively-induced turbulence (CIT) are quite similar. That is not to say that we are claiming to develop a paradigm that includes a scale contraction process achieving the turbulent ‘‘event’’. Our goal is to develop a paradigm that synthesizes a recurring sequence of processes from the subsynoptic to meso-β scales of atmospheric motion. This paradigm will define the roles of frontogenesis, vorticity tendencies, and most importantly, ageostrophic motions in focusing a streamwise relative vorticity gradient maximum accompanying an ageostrophically-forced front in the location of an observed severe turbulence event. We are seeking to understand the hydrostatic ageostrophic environment responsible for organizing severe turbulence. The seminal flow regime that is key to the aforementioned paradigm is that associated with supergradient wind flow. By supergradient wind flow we mean flow that significantly exceeds gradient wind balance due to the large magnitude of the centrifugal force. Supergradient wind flow facilitates a rapid increase in mesoscale frontogenetical forcing by increasing the ageostrophic

confluence prior to the development of nonhydrostatic convective forcing. By ''frontogenetical forcing'' we mean nonlinear processes that increase the magnitude of a streamwise mesoscale front. Supergradient and unbalanced supergradient wind flows are very effective at increasing streamwise wind perturbations as the ageostrophic confluence accompanying said flows is often frontogenetical, thus producing along-stream temperature (density) gradients in proximity to along-stream mass (pressure) perturbations. From an isentropic perspective this represents the convergence of streamwise ageostrophic relative vorticity on a sloping isentropic surface in a buoyant environment. Such a circulation establishes an environment that is favorable for the forcing of latitudinal and longitudinal vorticity through streamwise gradients of the 3D-wind field components, i.e., ageostrophic flow conducive to microscale vortex tube formation. Microscale vortices act to focus well-mixed and high velocity regions of turbulence.

In the following section we will briefly describe the four case studies to be simulated that are representative of aircraft accident-producing clear air and convective turbulence, and which are analogous to those analyzed in Kaplan et al (2003). We will also describe the numerical model and simulation experiments employed to understand the key sequence of ageostrophic processes, which we will subsequently describe. Section 3 will focus on the meso-α scale ($\sim$500 km) structure of the intersecting confluent jet streak entrance regions, which organize the key hydrostatic severe turbulence-forcing processes presented in Sect. 4. It is the highly ageostrophic flows created by these juxtaposed jet entrance region circulations that organize the potential for supergradient wind flow that leads to meso-β scale ageostrophically-forced frontogenesis accompanying streamwise ageostrophic relative vorticity. In Sect. 4, we will describe stage 1 of the overall paradigm, wherein meso-β scale ($\sim$100 km) ageostrophic forcing organizes frontogenesis. This involves the development of supergradient wind flow within two laterally and vertically juxtaposed jet entrance region circulations. In Sect. 5, we will summarize the new hydrostatic component of the severe turbulence-producing paradigm.

2. Model simulation experiments

2.1 Numerical model

The numerical model employed in our hydrostatic real data simulation experiments is the Mesoscale Atmospheric Simulation System (MASS) (e.g., Kaplan et al, 2000). Table 1 describes the characteristics of version 5.13. The hydrostatic simulations, to be described in the following sections, are the 30 km (coarse) and 6 km (fine) mesh resolutions. Initial and time dependent lateral boundary conditions are derived from the National Weather Service (NWS) Eta analyses for the coarse mesh simulation. All subsequent finer scale simulations, which are nested, derive their initial and time dependent lateral boundary conditions from the previous coarser mesh simulation. Climatological soil moisture and sea surface temperatures as well as an average of both silhouette and envelope terrain are utilized in all four simulated case studies. Representative matrix sizes employed, initialization times, and other key details are defined in Table 2.

2.2 Severe turbulence case studies

Two of these four real data case studies represent accident-producing/severe turbulence events as described in the archives of the National Transportation Safety Board (NTSB) analogous to those presented in Kaplan et al (2003). Table 3 defines the details of the turbulence encounter time and location and Fig. 1e graphically depicts their locations. One of the four case studies unambiguously occurs in clear air about 50 km southwest of Cape Girardeau, Missouri (CGI) at 1453 UTC 28 January 1997 at nearly 7 km elevation. This represents one of the two accident case studies. The other three case studies are all in proximity to moist convection. Two of these involve deep moist convection, the first of which occurred about 60 km southwest of Cross City, Florida (CTY) at 0045 UTC 2 October 1997 at around 10 km, which is the second accident case study. The other deep convection case is NASA-Langley Flight Experiment 191 about 90 km southwest of Valdosta, Georgia (VAD) at 1844 UTC 14 December 2000 at around 10 km. The fourth case study represented an

Table 1. MASS model (vers. 5.13) characteristics

Model Numerics:

- Hydrostatic primitive equation model
- 3-D equations for u, v, T, q, and p
- Cartesian grid on a polar stereographic map
- Sigma-p terrain-following vertical coordinate
- Vertical coverage from ∼10 m to ∼16,000 m
- Energy-absorbing sponge layer near model top
- Fourth-order horizontal space differencing on an unstaggered grid
- Split-explicit time integration schemes: (a) forward-backward for the gravity mode and (b) Adams-Bashforth for the advective mode
- Time-dependent lateral boundary conditions
- Positive-definite advection scheme for the scalar variables
- Massless tracer equations for ozone and aerosol transport

Initialization:

- First guess from large-scale gridded analyses
- Reanalysis with rawinsonde and surface data using a 3D optimum interpolation scheme
- High-resolution terrain data base derived from observations
- High-resolution satellite or climatological sea surface temperature database
- High-resolution land use classification scheme
- High-resolution climatological subsoil moisture data base derived from antecedent precipitation
- High resolution normalized difference vegetation index

Pbl Specification:

- Blackadar PBL scheme
- Surface energy budget
- Soil hydrology scheme
- Atmospheric radiation attenuation scheme

Moisture Physics:

- Grid-scale prognostic equations for cloud water and ice, rainwater, and snow
- Kain-Fritsch convective parameterization

Table 2. Data for the four hydrostatic simulations

Case	Horizontal resolution	Vertical resolution	Initialization time	Grid dimensions
Cape Girardeau				
simulation 1	30 km	45	0000 UTC 1/28/97	130 × 100
simulation 2	12 km	45	0600 UTC 1/28/97	130 × 100
simulation 3	6 km	60	1000 UTC 1/28/97	200 × 200
Valdosta				
simulation 1	30 km	50	0000 UTC 12/14/00	100 × 100
simulation 2	6 km	50	1000 UTC 12/14/00	100 × 100
Cross City				
simulation 1	30 km	35	0000 UTC 10/1/97	140 × 130
simulation 2	18 km	35	0000 UTC 10/1/97	140 × 130
simulation 3	6 km	35	1500 UTC 10/1/97	120 × 100
Wilmington				
simulation 1	30 km	50	0000 UTC 1/13/00	100 × 100
simulation 2	15 km	50	0600 UTC 1/13/00	170 × 170
simulation 3	6 km	50	1200 UTC 1/13/00	200 × 200

Table 3. Information about the turbulence encounter for each of the four case studies

Approximate accident location	Date	Time of turbulence encounter	Pressure level of turbulence
Cape Girardeau, Mo	1/28/97	1453 UTC	400 mb
Valdosta, Ga	12/14/00	1844 UTC	250 mb
Cross City, Fl	10/2/97	0045 UTC	275 mb
Wilmington, De	1/13/00	1931 UTC	775 mb

FAA Flight Operations Quality Assurance (FOQA) case study wherein equipment capable of recording severe turbulence was on board a commercial aircraft. This was the only low-level turbulence case study, occurring at around 2.4 km at 1931 UTC 13 January 2000 nearly 50 km southeast of Wilmington, Delaware (ILG) in proximity to relatively shallow convection. All of these case studies contain the same general synoptic scale atmospheric structure representative of most of the 44 case studies presented in Kaplan et al (2003), namely, a jet entrance region, upstream curvature accompanying streamwise gradients of ageostrophic relative vorticity, nearby convection (except the clear air case study), upward synoptic scale vertical motion, low absolute vorticity, horizontal cold air advection, and synoptic scale leftward-directed ageostrophic flow. The VAD and ILG case studies likely could have been ''accident-producing'' events as defined in Kaplan et al (2003) were there not special circumstances involved in the observation of severe turbulence, which did occur. CGI differs from the other three case studies in that there was no moist convection near the accident event. These 4 case studies were not included in the 44-case study sample described in Kaplan et al (2003). These four case studies were selected for the comprehensive modeling studies described in this paper and in a subsequent paper, because of the detailed flight data recorder information, which NASA was able to access for these cases from either the NTSB or actual experimental research flights. Almost all of the 44 case studies described in Kaplan et al (2003) did not have any accessible high-quality flight data recorder information. Hence, the validation of the modeling of these 4 case studies from subsequent Large Eddy Simulation (LES) studies is facilitated by microscale observations of the dynamics preceding the turbulent event as diagnosed from the flight data recorder information.

3. Converging meso-α scale jet streak entrance regions

Figures 1–3 depict the observed synoptic National Centers for Environmental Prediction (NCEP) Eta analysis fields valid at the rawinsonde time immediately preceding the severe turbulence event with the exception of the ILG case study (where the data follow the event). The times of the observational analyses are the closest possible to the times of the accidents or observations of severe turbulence. Figure 4 depicts important 30-km simulated dynamical fields accompanying the jet streams for all 4 case studies, while Figs. 5–6 focus on the two case studies with the strongest jet streams. These figures of simulated data include horizontal cross sections of winds and heights near the elevation of severe turbulence (Fig. 4) as well as jet axis perpendicular vertical cross sections of winds (Fig. 5) and isentropic potential vorticity (IPV) (Fig. 6). The times of each simulated cross section are about 1–2 hours prior to the observed severe turbulent event. These case studies vary substantially in the intensity of the meso-α scale jet streams near the accident

Fig. 1. NCEP Eta analysis observed total wind isotachs (dashed in ms^{-1}) and heights (solid in m) for the mandatory pressure level and valid at the observation time preceding the accident for the (**a**) CGI case study at 400 hPa and valid at 1200 UTC 28 January 1997, (**b**) ILG case study at 850 hPa and valid at 0000 UTC 14 January 2000, (**c**) CTY case study at 250 hPa and valid at 0000 UTC 2 October 1997, and (**d**) VLD case study at 250 hPa and valid at 1200 UTC 14 December 2000. (**e**) Locations of turbulence reports for the 4 case studies. Number 1 represents the 28 January 1997 Cape Girardeau, MO (CGI) case. Number 2 represents the 14 December 1997 Valdosta, GA (VLD) case. Number 3 represents the 2 October 1997 Cross City, FL (CTY) case. Number 4 represents the 13 January 2000 Wilmington, DE (ILG) case

locations, with the CGI case study jet being the strongest, but there are many common signals among the various cases. First, they represent the region in between two jet stream entrance regions and their supporting baroclinic zones. The jet streak entrance regions are juxtaposed

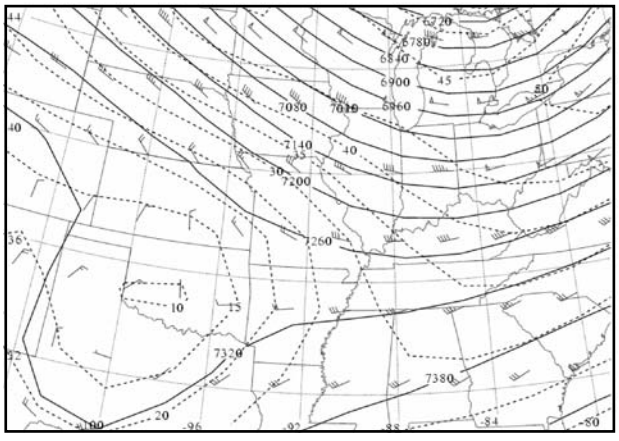

a

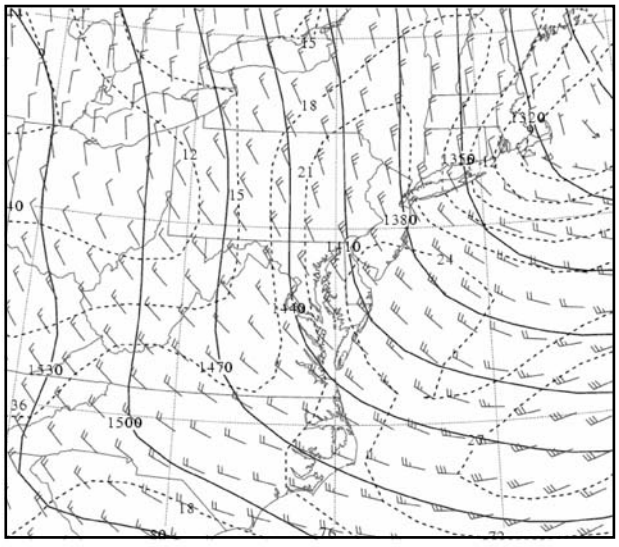

b

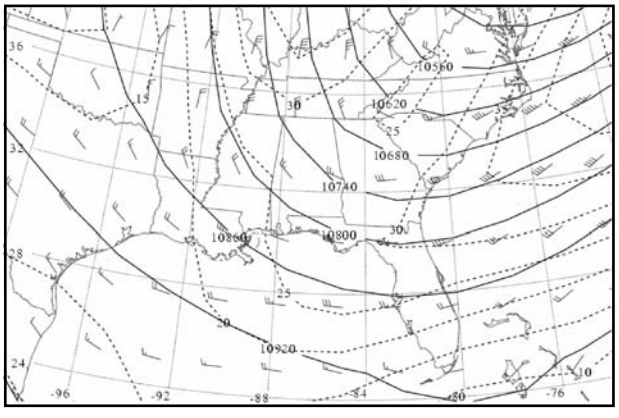

c

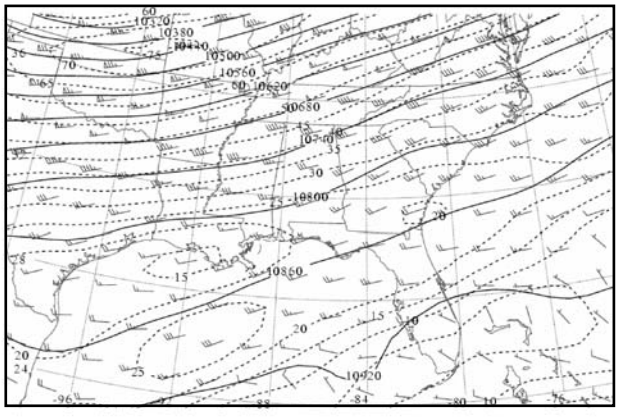

d

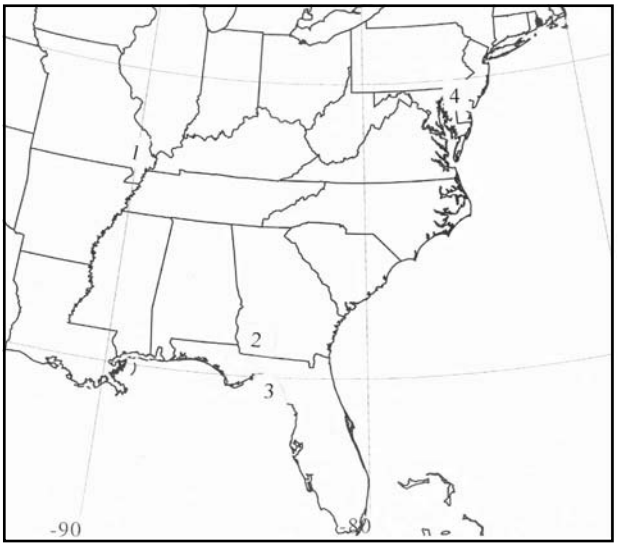

e

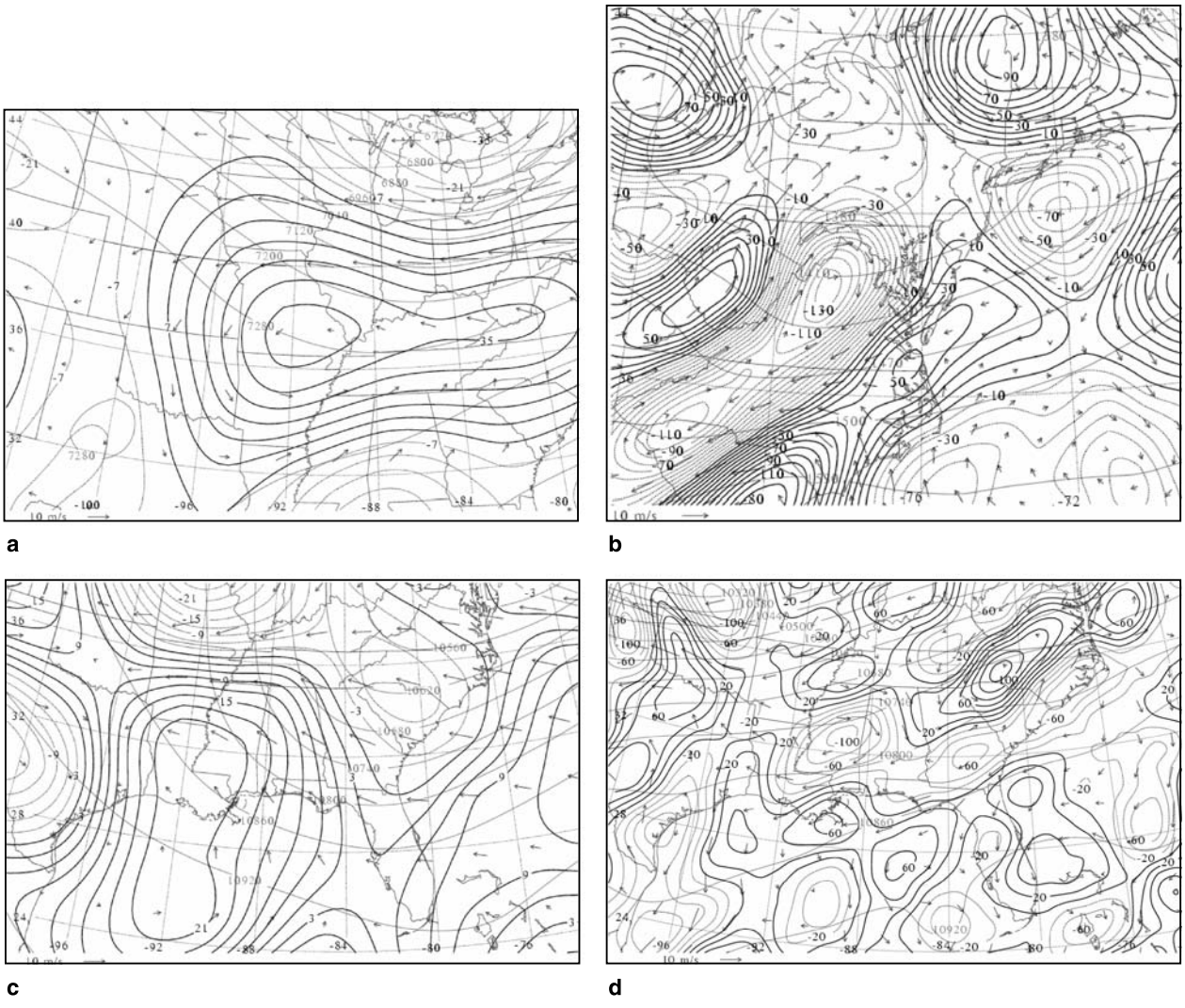

Fig. 2. NCEP height (light solid in m), ageostrophic wind vectors, and ageostrophic relative vorticity (negative dashed and positive dark solid in $s^{-1} \times 10^{-6}$); (**a**) NCEP Reanalysis 400 hPa 1200 UTC 28 January 1997, (**b**) Eta 850 hPa 0000 UTC 14 January 2000, (**c**) NCEP Reanalysis 250 hPa 0000 UTC 2 October 1997, and (**d**) Eta 250 hPa 1200 UTC 14 December 2000

vertically and horizontally. The northern stream is curved, weaker, and lower in elevation while the southern stream is straighter, stronger, and higher in elevation (Figs. 1 and 4). Second, these jet stream entrance regions indicate highly confluent ageostrophic flow with leftward-directed ageostrophy in the southern jet stream and rightward-directed ageostrophy in the northern jet stream (as can be seen in the ageostrophic wind vectors depicted in Fig. 2 and inferred from the wind and height data depicted in Fig. 4). Third, the vertical structure depicted in Fig. 5 indicates a wind maximum above and just upstream from the level of the accident, with a region of stronger winds extending downward through the level of the accident (indicating the proximity of the deep vertically phased jet streams). Fourth, a separate weaker IPV maximum (Fig. 6), which is in proximity to the accident location in both space and time, slopes downwards and is detached from a more classic stratospheric IPV maximum accompanying a tropopause fold. The IPV maximum near the level of the severe turbulence event is located within the transition zone between the jet stream entrance regions. The low altitude and separate structure of these IPV maxima infer a separate, highly ageostrophic organizational process for their location and intensity, as these features do not directly accompany the deeper and much stronger, as well as larger, quasi-geostrophic tropopause folding event accompanying the injection of large-IPV stratospheric air. This

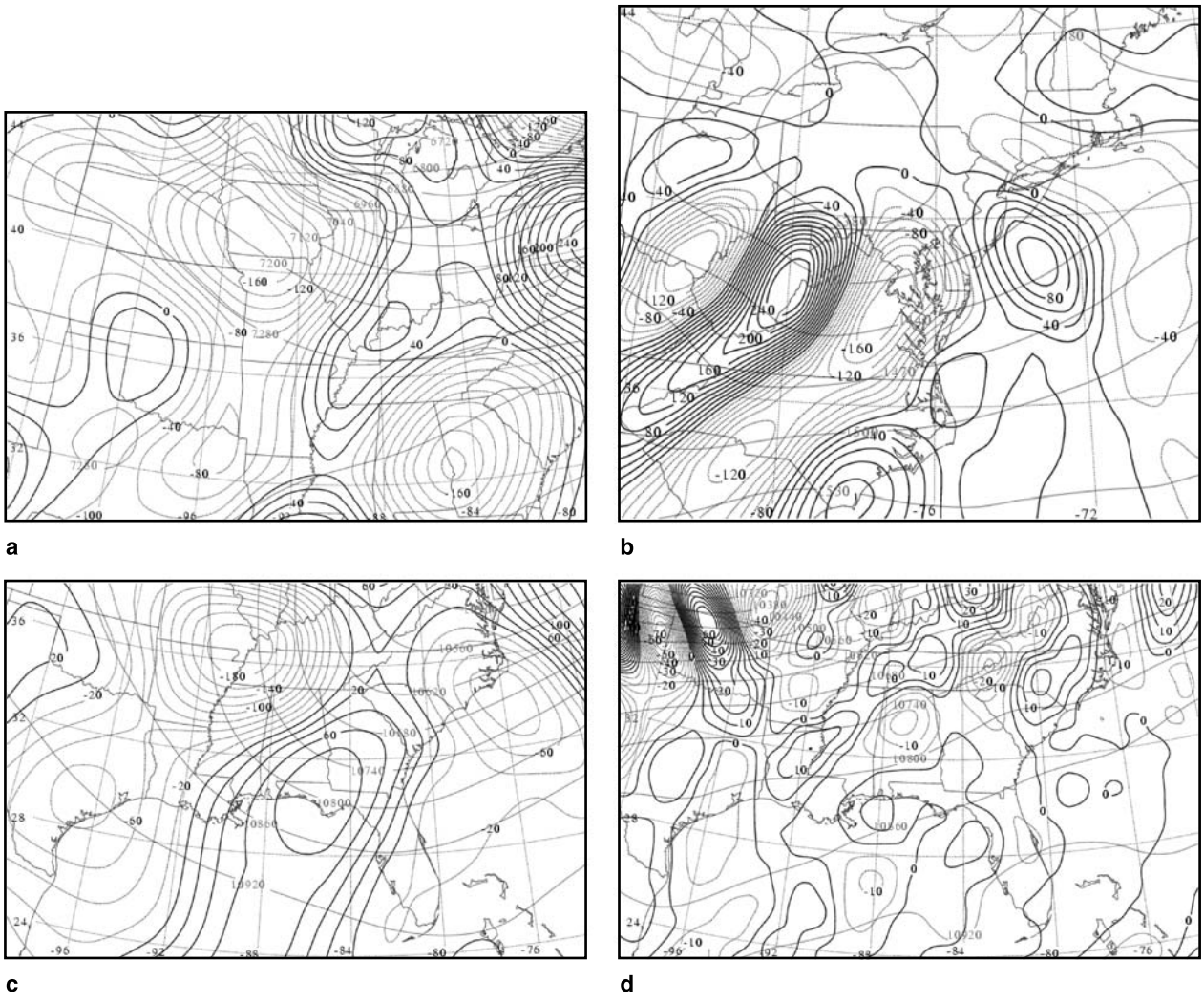

Fig. 3. NCEP height (light solid in m) and ageostrophic relative vorticity advection (negative dashed and positive dark solid in $s^{-2} \times 10^{-10}$); (**a**) NCEP Reanalysis 400 hPa 1200 UTC 28 January 1997, (**b**) Eta 850 hPa 0000 UTC 14 January 2000, (**c**) NCEP Reanalysis 250 hPa 0000 UTC 2 October 1997, and (**d**) Eta 250 hPa 1200 UTC 14 December 2000 ($s^{-2} \times 10^{-9}$)

indicates the possibility that a separate downstream and low-level frontogenetical circulation is being established that is detached from the quasi-geostrophic front (accompanying the tropopause fold within the thermally direct transverse ageostrophic circulation indicative of low Rossby number flow). Additionally, the ageostrophic circulation vectors (inferred from Fig. 2) accompanying the lower-level and weaker secondary IPV maximum, indicate highly different circulations in the two jet stream entrance regions in which a subsynoptic thermally indirect circulation exists poleward of a thermally direct circulation. Both of these entrance region circulations exhibit stronger horizontal accelerations than the upper-level primary IPV maximum does.

The most significant signals of the intersecting jet entrance regions and secondary IPV maxima are evident in the CGI and ILG case studies. Note, in particular, in these two case studies, how the ageostrophic confluence is being established between Arkansas and Illinois and Pennsylvania and Virginia, for CGI and ILG, respectively. The secondary IPV maxima align themselves rather closely with the accident location between these ageostrophic confluent regions. Furthermore, the ageostrophic wind vectors are separated by a region of highly curved flow in all 4 case studies, but most notably in the CGI and ILG case studies. Finally, and most dramatically, Figs. 2–3 indicate the dominance of streamwise gradients of ageostrophic relative

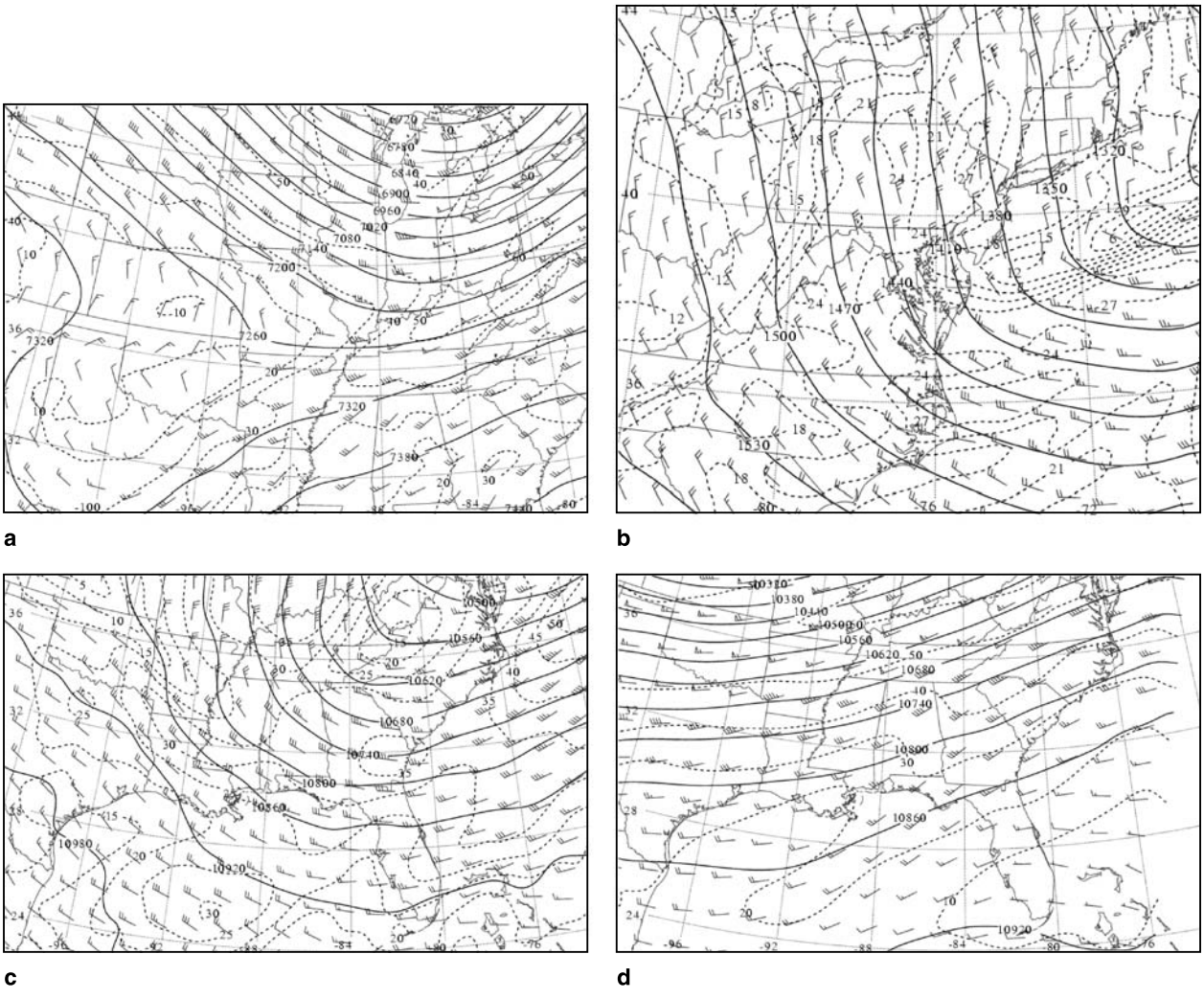

Fig. 4. MASS 30 km simulated total wind isotachs (dashed in ms^{-1}), wind barbs (short barb = 5 ms^{-1}; long barb = 10 ms^{-1}; triangle = 50 ms^{-1}), and heights (solid in m) valid on/at (**a**) 400 hPa 1200 UTC 28 January 1997, (**b**) 850 hPa 0000 UTC 14 January 2000, (**c**) 250 hPa 0000 UTC 2 October 1997, and (**d**) 250 hPa 1200 UTC 14 December 2000

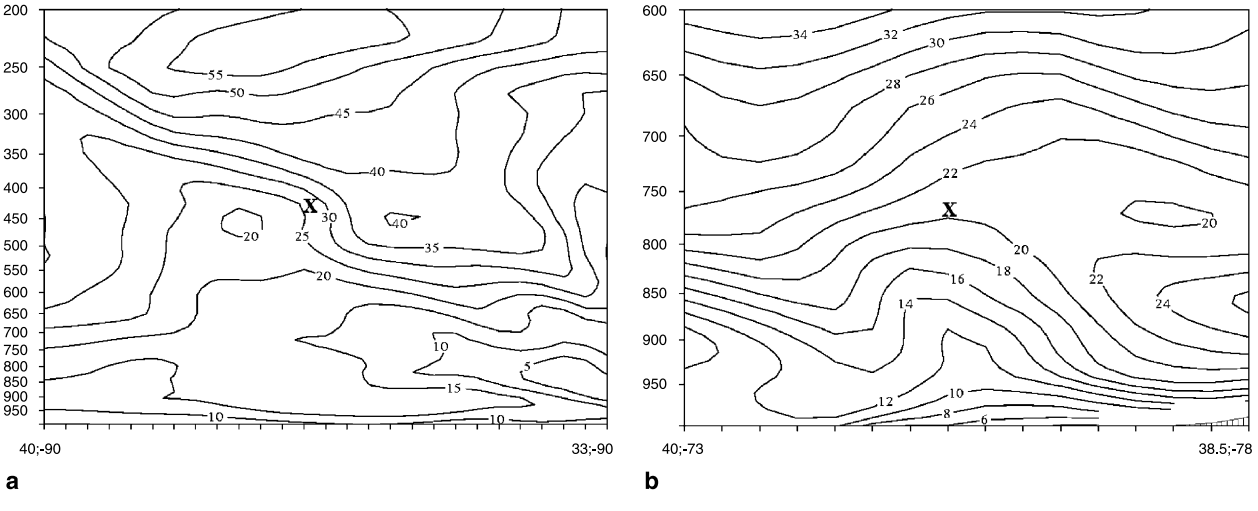

Fig. 5. MASS 30 km simulated jet normal vertical cross sections of total wind isotachs (solid in ms^{-1}) valid at (**a**) 1200 UTC 28 January 1997, (**b**) 1800 UTC 13 January 2000 (''X'' marks approximate accident location)

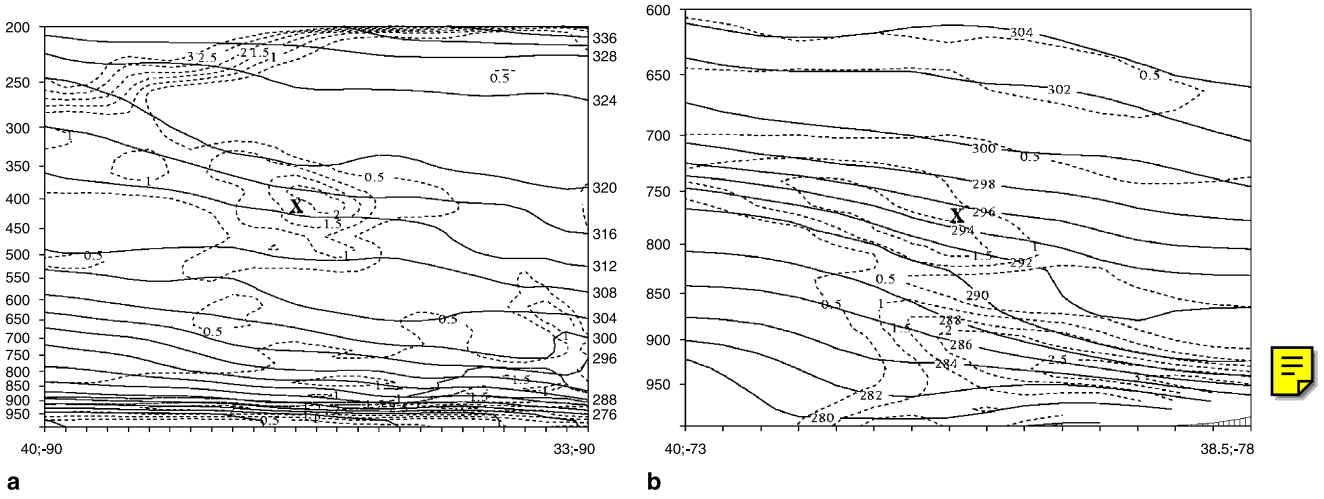

Fig. 6. MASS 30 km simulated jet normal vertical cross sections of potential temperature (solid in K) and isentropic potential vorticity (dashed in $\mathrm{Kmb^{-1}\,s^{-1}} \times 10^{-6}$) valid at (**a**) 1200 UTC 28 January 1997, (**b**) 1800 UTC 13 January 1997, (**c**) 0000 UTC 2 October 1997, and (**d**) 1800 UTC 14 December 1997. ("X" marks approximate accident location)

vorticity and ageostrophic relative vorticity advection in all four case studies. The streamwise gradients of vorticity and vorticity advection typically exceed the cross-stream gradients in magnitude near the accident location in the horizontal and level in the vertical. Additionally, a close look at the CGI and ILG case studies (the strongest case studies) indicates a signal of an observed ageostrophic cyclonic circulation (Fig. 2). This circulation is centered roughly on Missouri for CGI (Fig. 2a) and just offshore from the mid Atlantic coast southeast of ILG (Fig. 2b). This represents the juxtapositioning of a southern jet streak and its ageostrophic entrance region circulation and a northern jet streak and its ageostrophic entrance region circulation within an environment dominated by curved cyclonic ageostrophic flow.

The juxtapositioning of these two very different ageostrophic circulations is effective at forcing a region of ageostrophic confluence in proximity to the cold air that is typically located within the poleward jet stream entrance region. Hence, the circulations establish a favorable environment for ageostrophically-forced frontogenesis and fine-scale streamwise temperature/density gradients as confluence and temperature gradients are juxtaposed. These observed and simulated structures are consistent (in a synoptic sense) with the confluence occurring between two jet entrance regions upstream of a region of curved flow. Synoptic analyses of IPV and ageostrophic circulation vectors (not shown) can not match the detail necessary that is required to verify these features inherent in the 30 km simulations, thus indicating how subsynoptic and ageostrophic these features actually are.

4. Meso-β scale centripetally-forced ageostrophic vertical vorticity and frontogenesis in between the 2 jet streaks

Here we perform analyses employing the fields simulated with the 6-km hydrostatic version of the numerical model. Figure 7 depicts the simulated ageostrophy in the two strongest case studies on the pressure surface that is nearly coincident with the level of the accident. This ageostrophy is located in the region of curved flow where the more northern trough and the southern jet entrance region are juxtaposed. In all four case studies the simulated ageostrophic wind vectors have a similar pattern. This pattern of ageostrophic flow is somewhat like a positively (northeast–southwest) tilted cyclonic circulation roughly centered on the accident location. To the north and west of the accident location, the ageostrophic wind vectors are directed upstream of the large scale wind flow. To the south and east of the accident location they are directed downstream of the large scale flow. This is analogous to a positively tilted highly

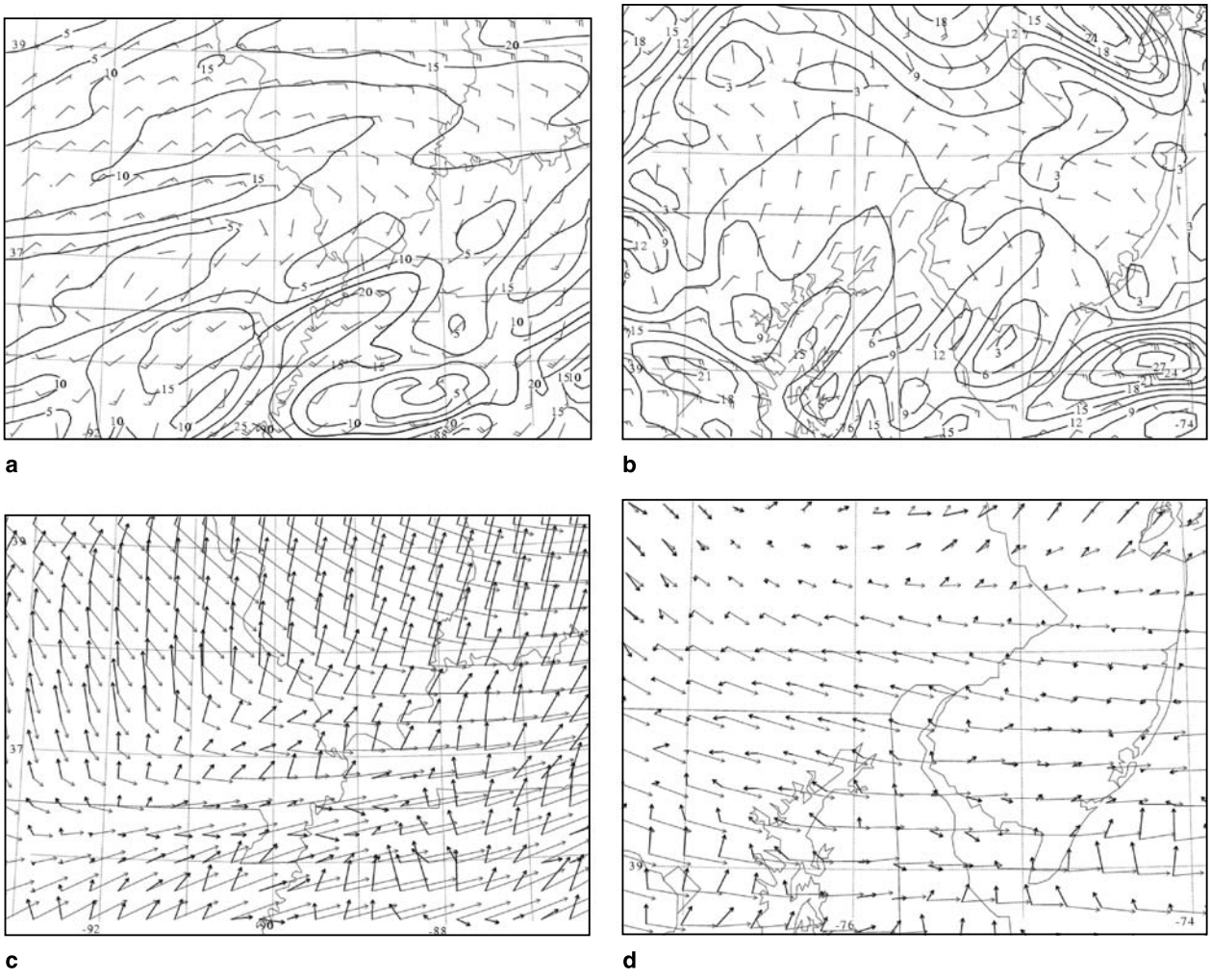

Fig. 7. MASS 6 km simulated ageostrophic wind isotachs (solid in ms^{-1}) and vectors valid on/at (**a**) 400 hPa 1330 UTC 28 January 1987, and (**b**) 775 hPa 1900 UTC 13 January 2000. MASS 6 km simulated vector resultant of the pressure gradient force and Coriolis force (thick) versus the total wind vectors (thin) valid at (**c**) 400 hPa 1330 UTC 28 January 1997, and (**d**) 775 hPa 1900 UTC 13 January 2000

confluent cyclonic circulation with a bias towards leftward-directed cross-stream ageostrophic flow. Not all of the vectors conform strictly to this state of ageostrophy, as the shorter the radius of curvature and the stronger the momentum in the merging jet streaks, the more the vectors are likely to split the flow into upstream and downstream ageostrophic wind components (note the CGI and ILG case studies). This simulated pattern depicted in Fig. 7 can be roughly compared to the observed ageostrophic wind vectors depicted in Fig. 2a, b wherein the cyclonic ageostrophic circulation with upstream-directed flow to the northwest and downstream-directed flow to the southeast is evident surrounding Missouri (Fig. 2a) and just offshore southeast of the DelMarVa Peninsula (Fig. 2b). In the CTY and VAD case studies (not shown) the wind vectors are not sufficiently ageostrophic to unambiguously split the flow and produce the cyclonic circulation as in the CGI and ILG case studies, although a weak signal of the split flow does exist. The fact that any vectors conform to this state of imbalance is an indication of just how misphased the pressure gradient and Coriolis forces are, as they fail to directly balance one another by $>15\,ms^{-1}$ in these two case studies. This lack of direct balancing can be better visualized in Fig. 7c, d by comparing the (1) vector resultant of the ageostrophic flow not including the centrifugal force, i.e., the acceleration vector for straight flow (combined pressure gradient and

Coriolis force) and (2) the total wind vectors. This pattern represents subgeostrophic flow on the upstream side (generally north and west) of the accident and supergeostrophic flow on the downstream side (generally south and east) of the accident. The cyclonic rotation of the combined pressure gradient force and Coriolis force vectors relative to the trough structure in the total wind velocity vector can be seen in Fig. 7c, d. This pattern is in place prior to any forcing from moist or dry convection. This type of misphasing between the pressure gradient force and Coriolis force favors a flow in which there is a net acceleration directed downstream and to the right of the split in the wind flow well ahead of the trough and a net acceleration directed upstream and to the left of the split in the wind flow within the trough. This split in the ageostrophic flow produces ageostrophic vectors directed, in large part, along the stream but in opposite directions. When curvature of the wind flow is added to the imbalance of forces the centrifugal force is very effective at enhancing the net accelerations primarily directed downstream but with the maximum shifted upstream from the Coriolis force. As a matter of fact, the most highly curved flow is situated approximately between the upstream-directed maxima in the pressure gradient force and downstream-directed maxima in the Coriolis force, thus dominating the transition between the maxima of the two forces.

To diagnose the specific cause of this pattern of extreme ageostrophy resulting in large part from the flow curvature, we calculate the Eulerian imbalance of forces for inviscid flow at staggered grid points on the same pressure surfaces as the previous ageostrophic wind vectors for the CGI and ILG case studies. This accelerative signal in the imbalance of forces is strongest in the CGI and ILG case studies, but is also apparent to a lesser extent in the deeper, stronger convective events, i.e., CTY and VAD (not shown). These imbalanced force fields for the CGI and ILG case studies are shown in Figs. 8–11. The purpose of this calculation is to determine the dominant instantaneous forcing at each grid point surrounding the accident location. All calculations of the centrifugal force are based on parcel trajectory curvature as defined in Dutton (1980). These figures indicate that the upstream subgeostrophy is the result of the strong upstream-directed normal and tangential components of the pressure gradient force accompanying the northern curved and highly confluent jet stream entrance region (Fig. 9). The trough structure and its positively tilted and highly confluent height gradient causes the pressure gradient force vector (the resultant of cross- and along-stream components) to be directed from the north–northwest to the west–northwest. This orientation is consistent with a strong streamwise component of the pressure gradient force accompanying the curved height field (as in subgeostrophic flow). The down-stream-directed supergeostrophic flow is coincident with the Coriolis force maxima accompanying the straight

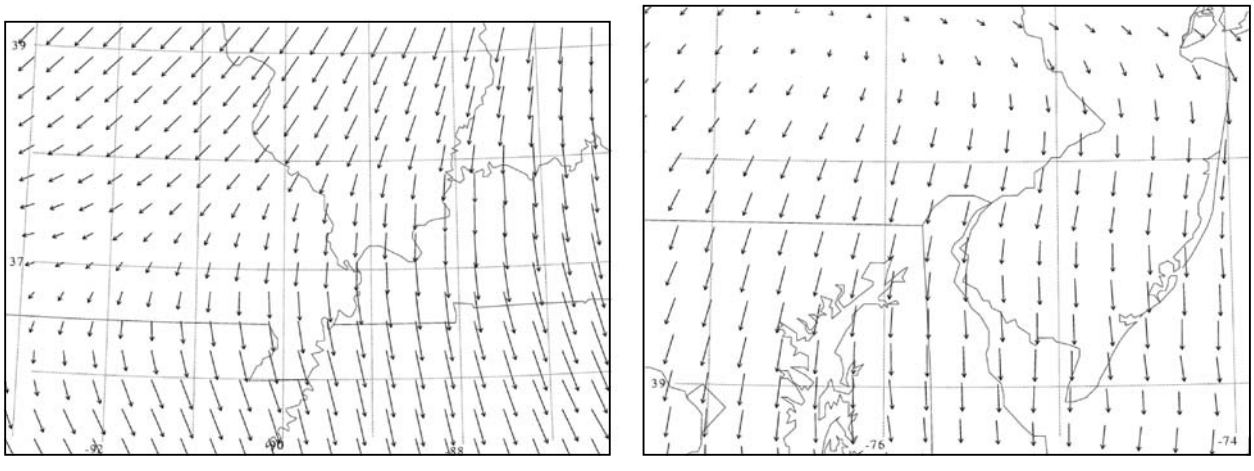

Fig. 8. MASS 6 km simulated Coriolis force vectors valid on/at (**a**) 400 hPa 1330 UTC 28 January 1997, and (**b**) 775 hPa 1900 UTC 13 January 2000

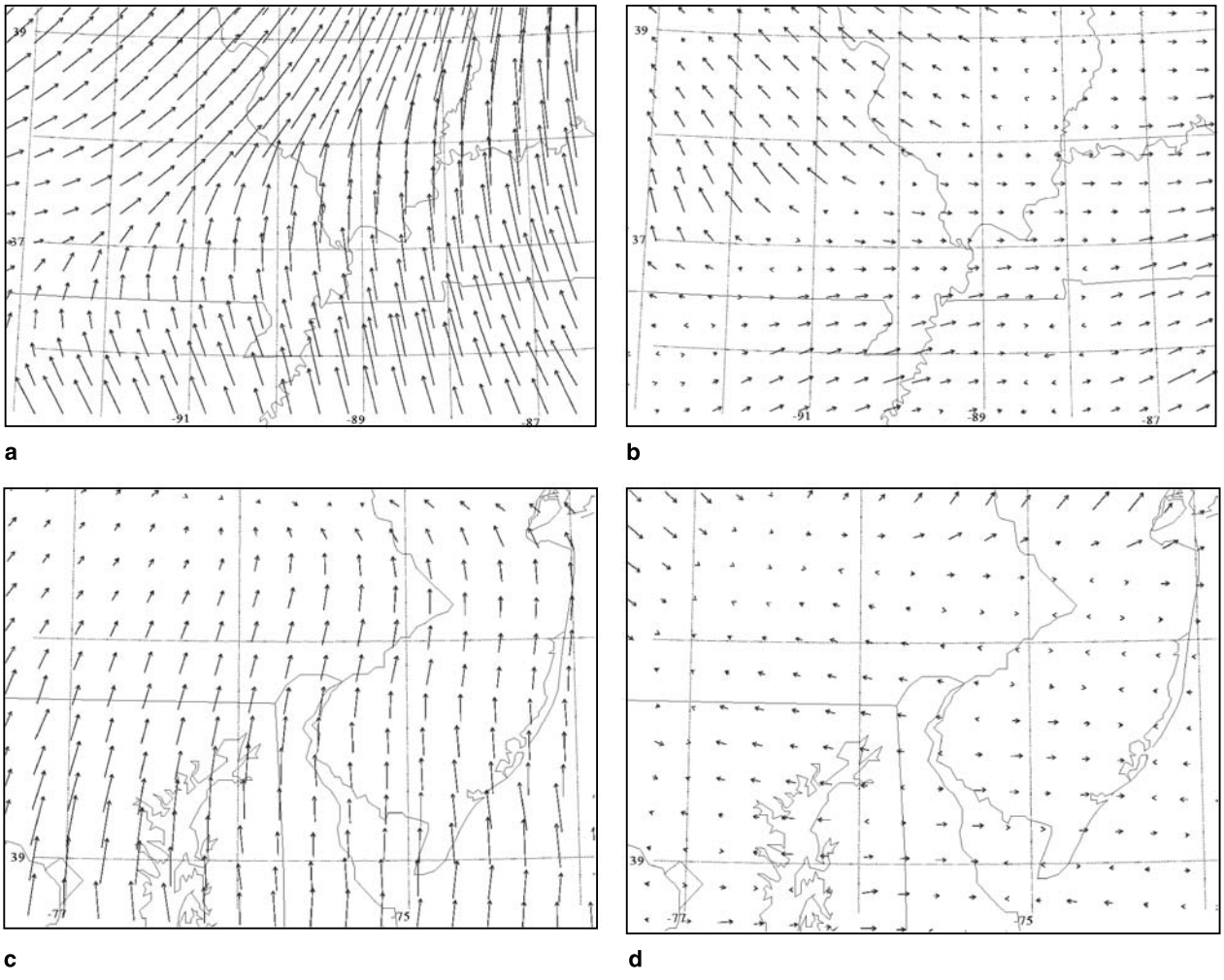

Fig. 9. MASS 6 km simulated cross-stream component and along-stream components of the pressure gradient force vectors valid on/at (**a**, **b**) 400 hPa 1330 UTC 28 January 1997, and (**c**, **d**) 775 hPa 1900 UTC 13 January 1997

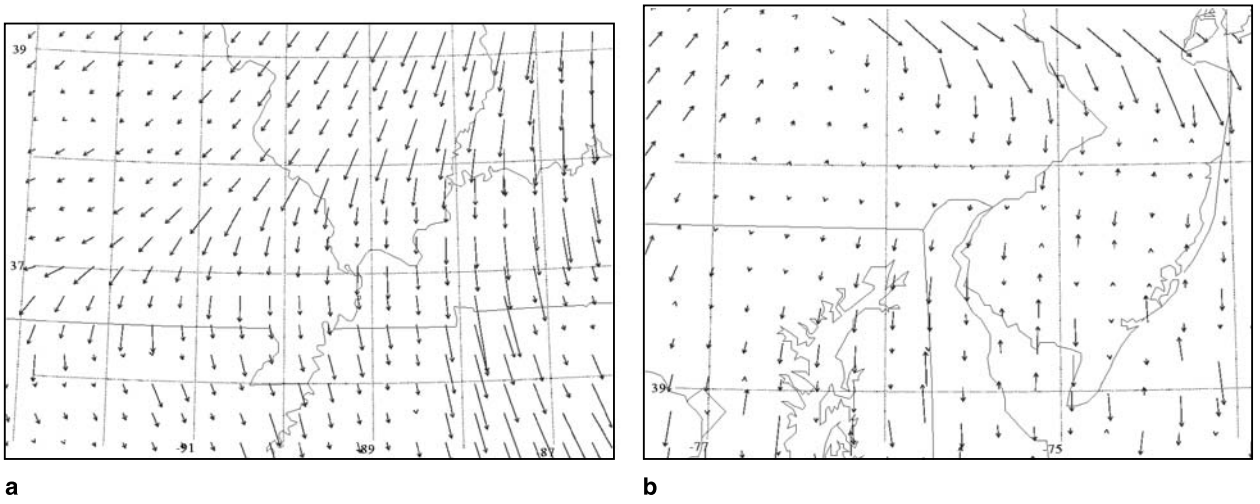

Fig. 10. MASS 6 km simulated centrifugal force vectors valid on/at (**a**) 400 hPa 1330 UTC 28 January 1997, and (**b**) 775 hPa 1900 UTC 13 January 2000

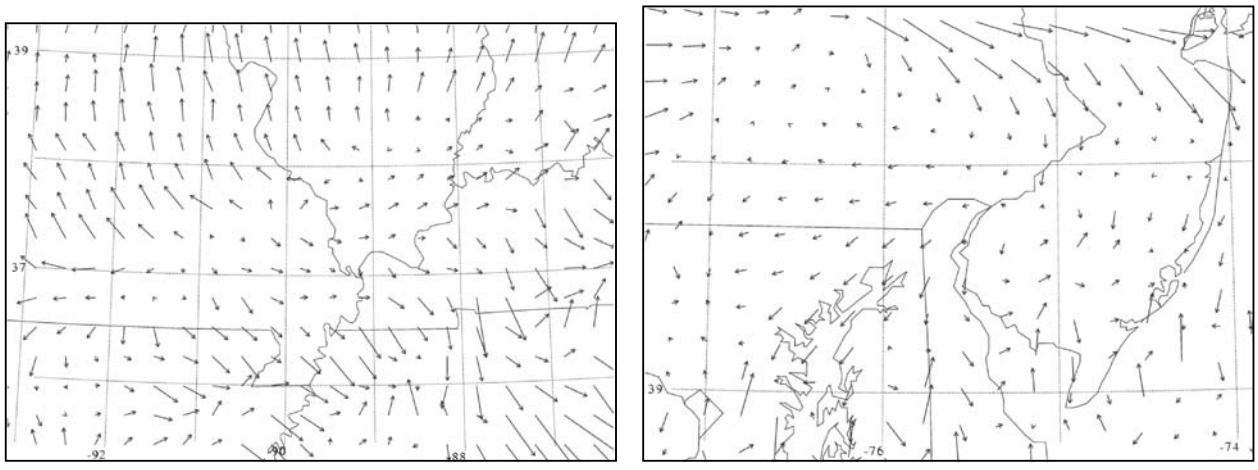

Fig. 11. MASS 6 km simulated resultant of all four force vectors valid on/at (**a**) 400 hPa 1330 UTC 28 January 1997, and (**b**) 775 hPa 1900 UTC 13 January 2000

southern jet streak entrance region where inertia-advection is very strong (Fig. 8). These two forces are spatially separated reflecting the proximity of a curved height field and straight jet stream flow. The region between the two aforementioned force maxima is generally a maximum in the centrifugal force with substantial centrifugal force variation (Fig. 10) as the radius of curvature is small and varying and the magnitude of the velocity is large. The resultant of all three forces (Fig. 11) is analogous to the pattern of ageostrophy depicted in Fig. 7, i.e., an acceleration vector but including curvature. Most important is the fact that the maxima in the along-stream pressure gradient force, cross-stream pressure gradient force, Coriolis force, and centrifugal force are all misphased, which facilitates the local variation of ageostrophy and the local dominance of centripetal flow between the large leftward (and upstream-directed) maxima of the pressure gradient force and large rightward (and downstream-directed) maxima of the Coriolis force. For example, note how the centrifugal force vector in Fig. 10 is greater in magnitude than the combined (1) pressure gradient force terms and (2) Coriolis vector resultant (Fig. 7) over the region between southern Missouri and western Kentucky for the CGI case study and over the region between northeastern Maryland, northern Delaware, and southwestern New Jersey for the ILG case study. The dominance of centripetal forcing is not as obvious in the CTY and VAD case studies, however, the pattern is similar (not shown).

This dominance of centripetal flow produces a narrow region where the flow may be termed supergradient (Figs. 9 and 10). Supergradient flow represents flow exceeding gradient wind balance due to large centripetal forcing, or flow having a small radius of curvature with large wind values. This supergradient flow is a result of the misphasing among all three terms established by the juxtaposition of these unique jet stream entrance region configurations and covers a meso-β scale region. The centrifugal force dominates any balance among the primary three forces responsible for inviscid flow allowing variation in curvature effects to control the frontogenetical and convergent forcing in the form of ageostrophic confluence over a very limited region during a short time period. The local supergradient flow maximum is very close to the turbulence accident location in all four case studies. The result is that the total wind's vertical vorticity gradient in this highly ageostrophic flow is not collocated with the geostrophic wind's vertical vorticity gradient, thus initiating the process of streamwise gradients of ageostrophic vertical vorticity. Centripetal forcing produces the streamwise shears that organize ageostrophic vertical vorticity maxima though convergence of vertical vorticity.

Meso-β scale spatial variations in the aforementioned centripetal forcing result in narrow

zones of enhanced velocity convergence and divergence as the ageostrophic vertical vorticity gradients increase over time. As such, one would expect that this pattern of ageostrophy, in proximity to the jet stream entrance region thermal variation, would represent a favored region for mesoscale rotational/ageostrophically-forced frontogenesis as thermal gradients and ageostrophic flow velocity convergence are large and coexist here. The aforementioned juxtaposition of ageostrophic confluent flow and temperature variation, that is required to produce frontogenesis can be inferred from Miller's (1950) equation below:

$$F = -\frac{1}{|\nabla\theta|}\left[\underbrace{\frac{\partial\theta}{\partial x}\left(\frac{\partial u}{\partial x}\frac{\partial\theta}{\partial x}+\frac{\partial u}{\partial y}\frac{\partial\theta}{\partial y}\right)}_{\mathrm{A}} + \underbrace{\frac{\partial\theta}{\partial y}\left(\frac{\partial v}{\partial x}\frac{\partial\theta}{\partial x}+\frac{\partial v}{\partial y}\frac{\partial\theta}{\partial y}\right)}_{\mathrm{B}} + \underbrace{\frac{\partial\theta}{\partial p}\left(\frac{\partial\omega}{\partial x}\frac{\partial\theta}{\partial x}+\frac{\partial\omega}{\partial y}\frac{\partial\theta}{\partial y}\right)}_{\mathrm{C}}\right]. \quad (1)$$

As the ageostrophy increases along the curved flow stream, note the dominance of the convergence term in (1), accompanying the streamwise variation of the predominantly ageostrophic v wind component (Fig. 12) within this region of strong centripetal forcing variation. This dominant ageostrophic contribution is coincident with the short length scale of the variation in centripetal forcing. The large streamwise variation of the ageostrophic wind is nearly coincident with the total frontogenesis (Fig. 14), which, in turn, passes very close to, if not over, the accident location in all four case studies. It is this particular forcing function (term B, above where v wind velocity gradients vary the most in magnitude) phasing with the larger-scale entrance region variation in the predominantly streamwise temperature variation (Fig. 13), which dominates the frontogenesis. In this region the longitudinal variation in the v ageostrophic wind velocity component consistent with the shearing deformation terms (not shown in Fig. 13), is much weaker in magnitude than the longitudinal variation in the u ageostrophic wind velocity component and the latitudinal variation of the v ageostrophic wind velocity component, i.e., the stretching deformation terms and their correlation with the NNW–SSE jet entrance region's temperature gradient (note Figs. 12–13). Confluence of the ageostrophic v wind component in the along-stream plane is coincident with the streamwise (WNW–ESE) component of the temperature variation, thus producing the dominant mesoscale frontogenetical forcing mechanism. The role of stretching deformation highlights the importance of the confluent cold trough as well as the large streamwise momentum

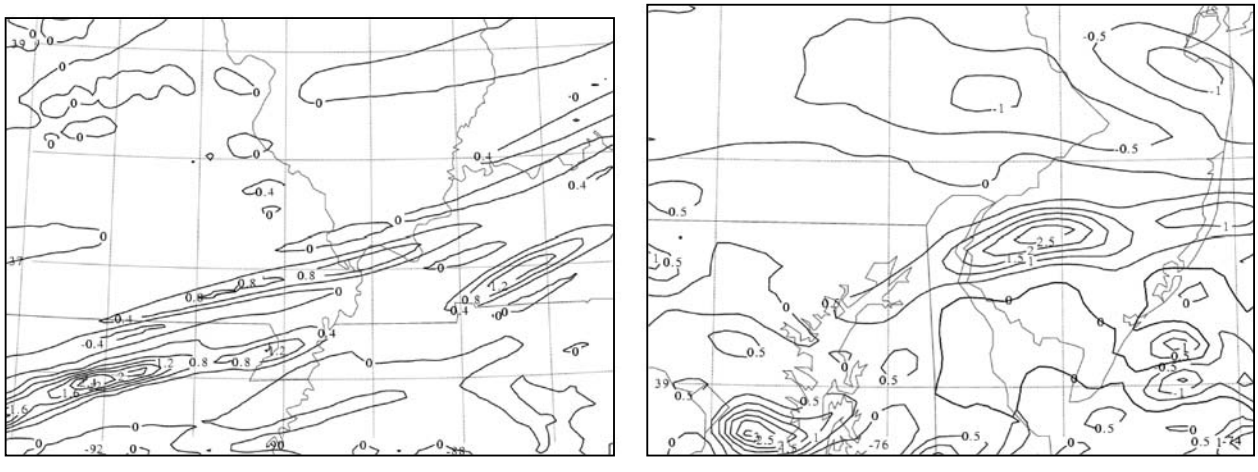

a b

Fig. 12. MASS 6 km simulated v wind component divergence forcing function term in Miller's frontogenesis equation ($\mathrm{Km^{-1}\,s^{-1}} \times 10^{-8}$) valid on/at (**a**) 400 hPa 1330 UTC 28 January 1997, and (**b**) 775 hPa 1900 UTC 13 January 2000

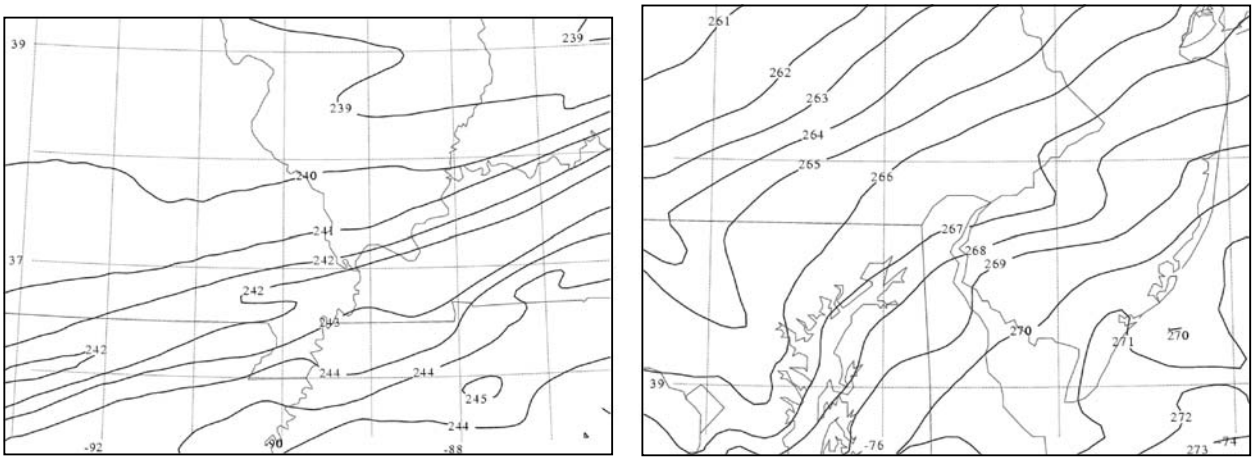

Fig. 13. MASS 6 km simulated temperature (K) valid on/at (**a**) 400 hPa 1330 UTC 28 January 1997, and (**b**) 775 hPa 1900 UTC 13 January 2000

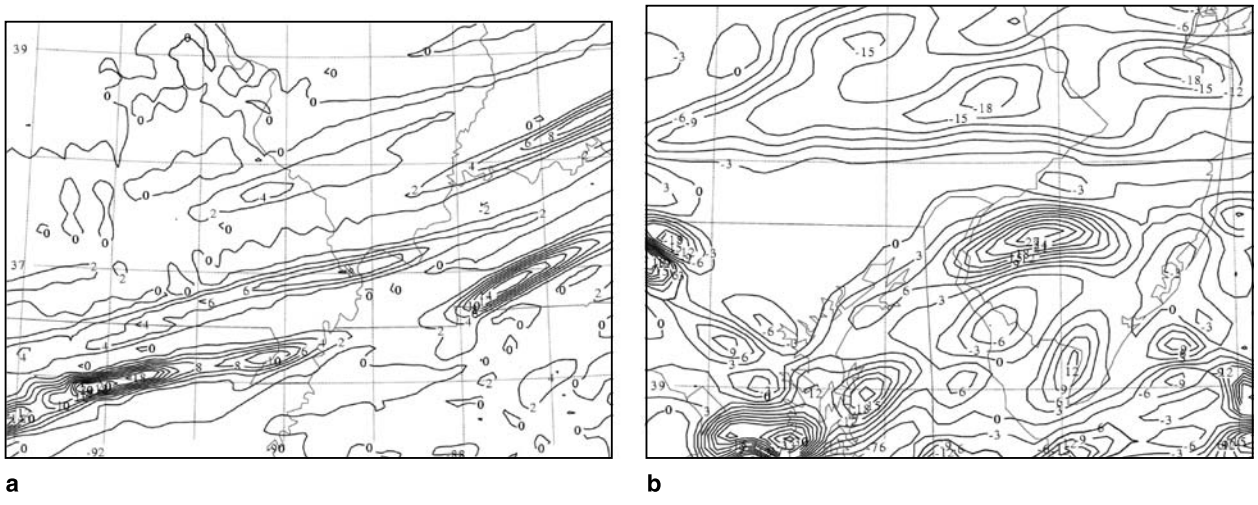

Fig. 14. MASS 6 km simulated total frontogenesis from Miller's (1957) equation ($Km^{-1}\,s^{-1} \times 10^{-8}$) valid on/at (**a**) 400 hPa 1330 UTC 28 January 1997, and (**b**) 775 hPa 1900 UTC 13 January 2000

variation typical of supergradient wind flow. The location of the confluent, ageostrophically-forced front is coincident with the transition from upstream-directed subgeostrophy to downstream-directed supergeostrophy. Hence, the frontogenesis is strongly controlled by the streamwise mesoscale variation in the curvature accompanying the ageostrophic wind and is roughly coincident with the accident location. This ageostrophic confluence results from the lateral variation of centripetal accelerative flow, which is allowed to occur in a largely unperturbed manner by the separated pressure gradient force (directed upstream) and Coriolis force (directed downstream) maxima in this uniquely-determined confluence zone between the two jet stream entrance regions. Centripetal forcing establishes the region of meridional confluence as the pressure gradient and Coriolis forces are directed at substantial angles to the centrifugal force by the confluence associated with two different jet stream entrance regions, i.e., one stream supplying curvature and cold air while the second stream supplies zonal momentum. The streamwise variation in the gradient of the ageostrophic vertical vorticity is coincident with

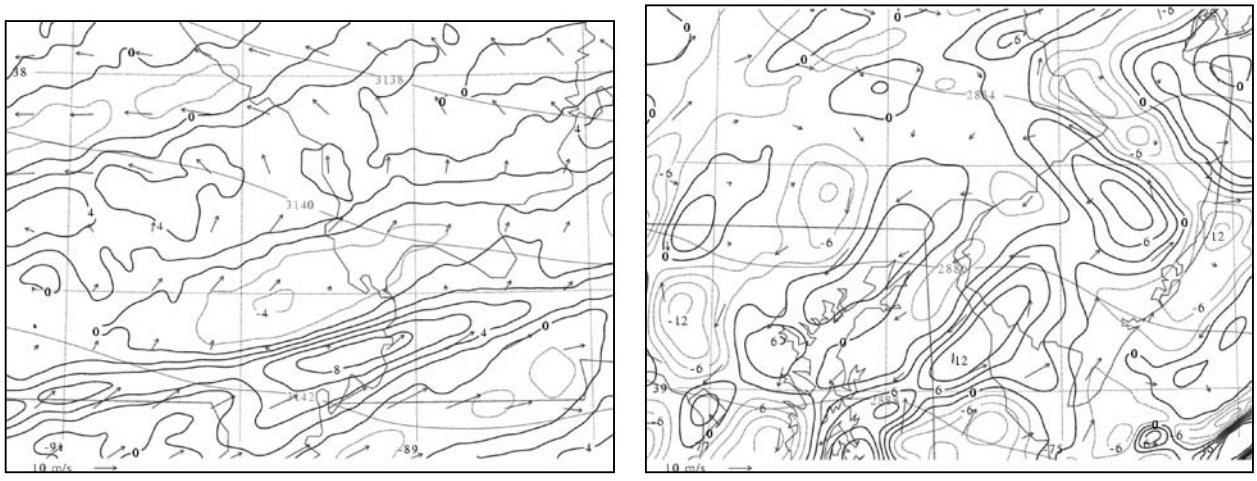

Fig. 15. MASS 6 km simulated Montgomery stream function (light solid in $m^2 s^{-2}$), ageostrophic wind vectors, and ageostrophic Z-space relative vorticity ($s^{-1} \times 10^{-4}$) valid on/at (**a**) 314 K 1330 UTC 28 January 1997, and (**b**) 287 K 1900 UTC 13 January 2000

the ageostrophic stretching deformation maxima. Hence, mesoscale frontogenesis in the curved flow acts to increase the angle between the streamwise ageostrophic vertical vorticity gradient and Montgomery stream function gradient as the slope of the isentropic surface, which accompanies the mesoscale frontogenesis, steepens. Frontogenesis and steepening isentropes become collocated with the streamwise ageostrophic vorticity gradient.

The narrow (~50–100 km) streamwise, ageostrophically-forced, front is therefore a region of intensifying ageostrophic vertical vorticity gradients on a sloping isentropic surface. Figure 15 depicts the ageostrophic vertical relative vorticity on the key isentropic surface passing through the location of observed turbulence both in the CGI and ILG case studies. Evident is the focusing of an ageostrophic vertical vorticity gradient maximum near the turbulence location, consistent with the narrow maximum in frontogenesis. This maximum in the gradient of ageostrophic vertical vorticity is also coincident with the maximum in ageostrophic deformation. This ageostrophic vorticity maximum is largely the result of the substantial velocity convergence in the centripetally forced streamwise confluence zone between the pressure gradient and Coriolis force maxima. The variation in centripetal forcing, its subsequent velocity convergence, and ageostrophic vertical vorticity are all phasing to produce a meso-β scale region of rapid density transition accompanying the newly-formed front (Figs. 13–14). As can be seen in Figs. 15 and 17, the location of the maxima of increasing ageostrophic vertical vorticity in time is close to the convergence/stretching term maxima in the vertical vorticity (calculated with the ageostrophic component of the wind in Fig. 14). As such, the vertical vorticity of the total wind and the vertical vorticity of the geostrophic wind can become separated with cyclonic ageostrophic vorticity shifted downstream relative to the cyclonic geostrophic vorticity. This produces a separate region of streamwise vertical vorticity gradient ahead of the larger scale trough within the newly formed front's sloping isentropes where increased buoyancy is being organized as well. Consistent with this are maxima in the variation in the advection of ageostrophic relative vorticity over southeastern Missouri and southwestern New Jersey for the CGI and ILG case studies, respectively (Fig. 16). These regions become dominated by a flow favoring streamwise ageostrophic vorticity advection. As such, the environment is becoming more conducive to horizontal vortex tube formation if a local source of buoyancy can tilt and converge this vertical vorticity into horizontal vorticity.

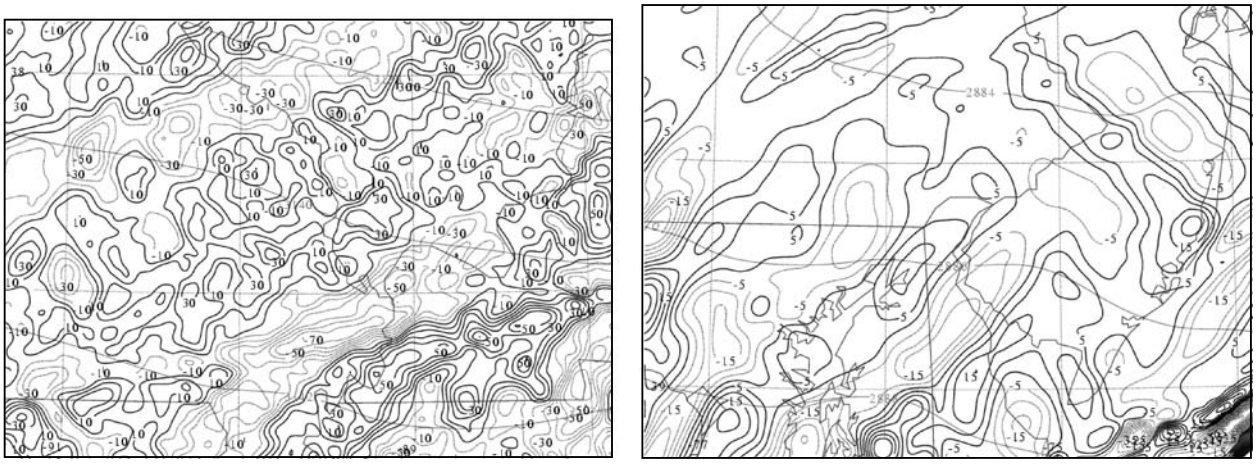

a b

Fig. 16. MASS 6 km simulated Montgomery stream function (light solid in $m^2 s^{-2}$) and the advection of ageostrophic Z-space relative vorticity ($s^{-1} \times 10^{-8}$) valid on/at (**c**) 314 K 1330 UTC 28 January 1997, and (**d**) 287 K 1900 UTC 13 January 2000

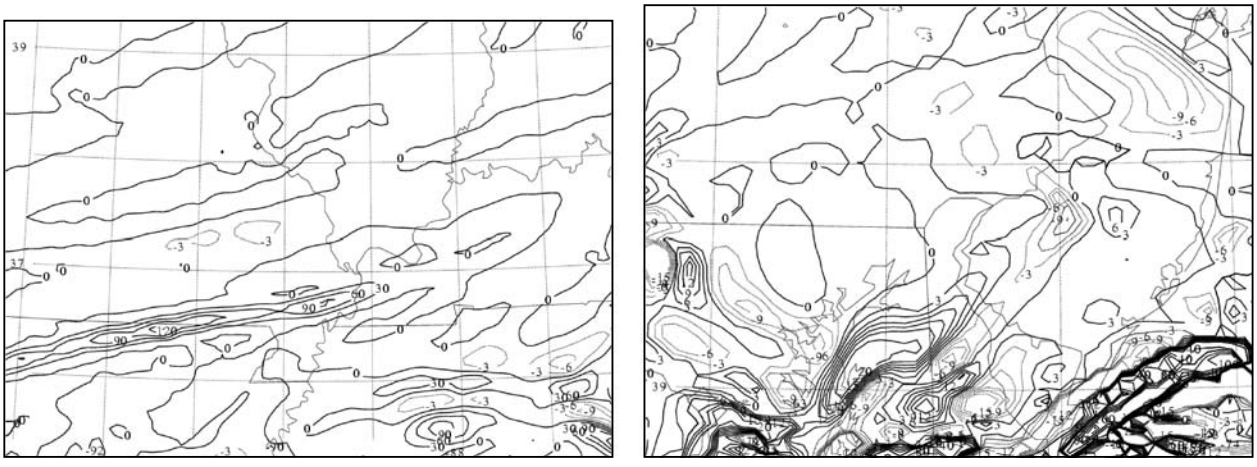

a b

Fig. 17. MASS 6 km simulated velocity divergence term in the ageostrophic Z-space relative vorticity equation ($s^{-2} \times 10^{-9}$ in a, $s^{-2} \times 10^{-7}$ in (**b**) on an isentropic surface valid on/at (**a**) 314 K 1330 UTC 28 January 1997, and (**b**) 287 K 1900 UTC 13 January 2000

5. Summary and discussion

The processes that separate the total vertical vorticity and geostrophic vertical vorticity maxima and create the intense streamwise front and accompanying ageostrophic vorticity gradients depicted in Figs. 13 and 15 have their roots in the meso-α jet streak structures. The juxtaposition of highly curved flow, cold air advection, and strong inertial-advective forcing set up an imbalance of forces that is highly ageostrophic. The signal of this ageostrophy is the fine scale confluence, which contracts the scale of the centripetally forced front and its attendant streamwise vertical vorticity maxima. This sequence of events is essentially about separating the geostrophic vertical vorticity from the total vertical vorticity creating the ageostrophic vertical vorticity on a sloping isentropic surface, i.e., the newly-formed ageostrophically-forced front and accompanying streamwise vorticity maxima. As such, the cross product formed by the gradients of the total vertical vorticity and the pressure gradient force should be large, indicating just how the ageostrophic front focuses this

separation. The pressure gradient force (gradient of Montgomery stream function) is progressively oriented more orthogonal to the gradients of ageostrophic vertical vorticity as indicated in Eq. (2), below:

$$\text{NCSU} = \nabla\zeta_\theta \times \nabla M_\theta, \tag{2}$$

where NCSU means North Carolina State University index. This separation of the horizontal pressure gradient force from the total vertical vorticity can be a multiscale indicator of the evolving ageostrophic frontogenesis and the convergence of vertical vorticity on folding isentropic surfaces. Hence, the separation is a potentially useful forecasting tool for the prediction of regions of severe turbulence potential. In its most basic representation, it is the location of most rapidly increasing streamwise vorticity gradient in a progressively more buoyant environment accompanying overturning isentropes. The increase of streamwise vertical vorticity will be where the total frontogenesis and ageostrophic vorticity are becoming collocated (as can be inferred from Figs. 13–17). The streamwise density gradient accompanying the newly formed front/ageostrophic vorticity maximum are becoming orthogonal to the streamwise pressure gradient force ahead of the trough in the mass field.

The hydrostatic mesoscale sequence of events hypothesized to maximize the potential for both clear air and convective turbulence is as follows:

(1) two jet stream entrance regions become juxtaposed, resulting in proximity to each other, i.e., curved flow in a baroclinic zone and stronger straight advective flow, which vary substantially in magnitude in the vertical,
(2) the misphasing of the along and cross-stream maxima in the pressure gradient force, the centrifugal force, and the Coriolis force at the interface of the two jet stream entrance regions produces a local region of highly confluent ageostrophic curved flow (which may be supergradient),
(3) the confluence resulting from the variation in the streamwise wind component in this highly ageostrophic ''stretched'' state in proximity to the cold air within the northern jet streak entrance region produces a meso-β scale frontal zone and accompanying maximum in ageostrophic vertical vorticity,
(4) the increasingly streamwise-oriented front becomes the locus of three-dimensional wind gradients and vertical vorticity (which are available for tilting) and vertical convergence into horizontally intensifying vortex tubes if significant buoyant lifting occurs.

From a 3D conceptual perspective, differential flow curvature acts to focus a front and thus force isentropic surfaces to overturn. As velocity convergence increases, any vertical vorticity is converged into the region of isentropic overturning. This produces an environment with significant rotation, 3D-wind shear and buoyancy in one focused location. Wave-induced overturning can focus vorticity in proximity to this location as Richardson numbers are low and rotation is large. As a result of these processes, rotating turbulent eddies are a likely byproduct.

This hydrostatic sequence of events results in the focusing of maxima of kinematic forcing, frontogenesis, and minima in Richardson number in the same place at the same time as the isentropic surface folds in proximity to strong 2-dimensional rotation about the vertical axis. From a physical perspective, this process represents isentropic surfaces folding over in proximity to strong gradients of ageostrophic vertical vorticity. Presumably, the turbulent event accompanies the breakdown of the flow established by this complex sequence of dynamical processes and the subsequent resulting sequence of non-hydrostatic adjustments which focuses vorticity (vortex tubes) in both the remaining horizontal (latitudinal and longitudinal) planes of motion. A potentially useful turbulence forecasting index that reflects these dynamics is developed, which is based on the misphasing of the geostrophic and total vertical vorticity gradients on an isentropic surface. Here the pressure gradient force is orthogonal to the gradient of vertical vorticity, thus contracting the scale of the front and streamwise vorticity gradients. The downscale growth of ageostrophy and frontogenesis is nothing more than the increasing orthogonality between the streamwise: (1) pressure gradient force and (2) gradient of total vertical vorticity.

In a subsequent paper, the second and third stages of this paradigm will be described using

both nested-grid real data nonhydrostatic simulations and idealized nonhydrostatic simulations of intense convectively-forced three-dimensional circulations. The scale contraction of the turbulence index from its hydrostatic maxima to finer scale nonhydrostatic maxima will be described in depth wherein buoyancy can lead to a set of adjustments that tilt and converge the newly formed streamwise vertical vorticity gradients at the hydrostatic scale of motion into horizontal vortex tubes at the nonhydrostatic scale of motion.

Acknowledgements

This research has been funded under NASA Contract #NAS1-99074 and Subcontract #82U-7473-008 from the Research Triangle Institute. The authors wish to acknowledge the support of Dr. Fred H. Proctor, the NASA-Langley Technical Contract Monitor and wish to thank the North Carolina Supercomputing Center for providing supercomputing time.

References

Andreassen O, Hvidsen PO, Fritts DC, Arendt S (1998) Vorticity dynamics in a breaking internal gravity wave. Part I: Initial instability evolution. J Fluid Mech 367: 27–46

Clark TL, Hall WD, Kerr RM, Middleton D, Radke L, Ralph FM, Nieman PJ, Levinson D (2000) Origins of aircraft-damaging clear air turbulence during the 9 December 1992 Colorado downslope windstorm: Numerical simulations and comparison to observation. J Atmos Sci 57: 1105–1131

Dutton MJO (1980) Probability forecasts of clear-air turbulence based on numerical model output. Meteorol Mag 109: 293–310

Ellrod GP, Knapp DI (1992) An objective clear air turbulence forecasting technique: Verification and operational use. Wea Forecast 7: 150–165

Endlich RM (1964) The mesoscale structure of some regions of clear-air turbulence. J Appl Meteor 3: 261–276

Gidel LT, Shapiro MA (1979) The role of clear air turbulence in the production of potential vorticity in the upper tropospheric jet stream-frontal systems. J Atmos Sci 36: 2125–2138

Kaplan ML, Lin Y-L, Charney JJ, Pfeiffer KD, Ensley DB, DeCroix DS, Weglarz RP (2000) A terminal area PBL prediction system at Dallas-Fort Worth and its application in simulating diurnal PBL jets. Bull Amer Meteor Soc 81: 2179–2204

Kaplan ML, Huffman AW, Lux KM, Charney JJ, Riordan AJ, Lin Y-L (2003) Characterizing the environment organizing severe accident-producing turbulence. Part I: A 44-case study synoptic observational analyses. Meterol Atmos Phys (forthcoming)

Keller JL (1990) Clear air turbulence as a response to meso and synoptic-scale dynamical processes. Mon Wea Rev 118: 2228–2242

Kennedy PJ, Shapiro MA (1980) Further encounters with clear air turbulence in research aircraft. J Atmos Sci 37: 986–993

Knox JA (1997) Possible mechanisms of clear-air turbulence in strongly anticyclonic flows. Mon Wea Rev 125: 1251–1259

Mancuso RL, Endlich RM (1966) Clear air turbulence frequency as a function of wind shear and deformation. Mon Wea Rev 94: 581–585

Marroquin A (1998) An advanced algorithm to diagnose atmospheric turbulence using numerical model output. Preprints, 16th AMS Conf. on Weather Analysis and Forecasting, 11–16 January 1998, Phoenix, AZ, pp 79–81

Parks EK, Wingrove RC, Bach RE, Mehta RS (1984) Identification of vortex-induced clear-air turbulence using airline flight records. J Aircraft 22: 124–129

Reed RJ, Hardy KR (1972) A case study of persistent intense clear air turbulence in an upper level frontal zone. J Appl Meteor 12: 541–549

Reiter ER, Nania A (1964) Jet stream structure and clear air turbulence. J Appl Meteor 3: 247–260

Roach WT (1970) On the influence of synoptic development on the production of high-level turbulence. Quart J Roy Meteor Soc 96: 413–429

Shapiro MA (1976) The role of turbulent heat flux in the generation of potential vorticity in the vicinity of upper-level jet stream systems. Mon Wea Rev 104: 892–906

Sharman R, Wiener G, Brown B (2000) Description and verification of the NCAR Integrated Turbulence Forecasting Algorithm (ITFA). AIAA 00-0493. AIAA 38th Aerospace Sciences Meeting and Exhibit, 10–13 January 2000, AIAA, Reno, NV

Stone PH (1966) On non-geostrophic baroclinic stability. J Atmos Sci 23: 390–400

Uccellini LW, Brill KF, Petersen RA, Keyser D, Aune R, Kocin PJ, des Jardins M (1986) A report on the upper-level wind conditions preceding and during the Shuttle Challenger (STS 51L) explosion. Bull Amer Meteor Soc 67: 1248–1265

Corresponding author's address: Prof. Yuh-Lang Lin, Department of Marine, Earth, and Atmospheric Sciences, Box 8208, North Carolina State University, Raleigh, North Carolina 27695-8208 (E-mail: yl_lin@ncsu.edu)

Dear Author,

The goal of our new, more rapid publication procedures is to publish your paper online as quickly as possible. The assigning of a DOI (digital object identifier) at this stage means that the work is fully citeable much earlier than has previously been the case. Please note that final pagination will be added only when articles have been assigned to a printed issue. With respect to the quality of figures in the electronic version, please note that the printed version will be of the usual high quality. For a list of all papers published online so far, please refer to the following web-site (your paper will be added to this list after final correction):

http://link.springer.de/link/service/journals/00703/tocs.htm

Offprint Order

Journal: Meteorology and Atmospheric Physics MS No.: 0/660 First Author: M. L. Kaplan

We will supply the corresponding author with one free copy of the relevant issue.
The order of offprints against payment must be sent in when returning the corrected proofs.
The prices quoted are valid only for authors ordering offprints for their private use.
Please write clearly in capital letters!

NEW **When you order offprints against payment, you are entitled to receive in addition a pdf file of your article for your own personal use.** As this pdf file is sent to you by e-mail, please insert the e-mail address here: _____

I hereby order against payment

☐ **50** ☐ **100** ☐ **200** ☐ **300** ☐ **400** **offprints**

Offprints should be sent to: _____
(Name of person or institution)

_____
(Address)

_____

Payment will be made by: _____
(Name of person or institution)

_____
(Address)

_____

(Purchase Order No.) _____ (Date/Signature of author) _____

☐ Please bill me **(please do not pay for offprints before receipt of invoice!)**

☐ Please charge my credit card ☐ Eurocard / Mastercard ☐ American Express
☐ Visa ☐ Diners Club

No.: |_|_|_|_|_|_|_|_|_|_|_|_|_|_|_|_| Valid until: |_|_|/|_|_|

Signature: _____

(In all separate correspondence concerning this order please quote the Journal's title, MS No., and First Author.)

Price list for offprints* Prices include carriage charges (surface mail). Prices are subject to change without notice.

***Customers in foreign EU countries:** Please state your V.A.T. registration number if applicable. Otherwise we have to add 10% V.A.T. to the list prices.

V.A.T. registration number: _____

Pages (Figs. incl./excl.)	50 Copies	100 Copies	200 Copies	300 Copies	400 Copies
	EUR	EUR	EUR	EUR	EUR
☐ 1–8	296,–	348,–	482,–	598,–	722,–
☐ 9–16	384,–	436,–	626,–	806,–	998,–
☐ 17–24	462,–	512,–	742,–	972,–	1198,–
☐ 25–32	512,–	564,–	844,–	1098,–	1408,–

Copyright Transfer Statement

The copyright to this article is hereby transferred to Springer-Verlag (for US Government employees: to the extent transferable), effective if and when the article is accepted for publication. The copyright transfer covers the exclusive rights to reproduce and distribute the article, including reprints, photographic reproductions, microform, electronic database, videodiscs, or any other reproductions of similar nature, and translations.
However, the authors reserve:

1. All proprietary rights other than copyrights, such as patent rights.
2. The right to use all or part of this article in future works of their own and to grant or refuse permission to third parties to republish all or part of the article or translations thereof. To republish whole articles, such third parties must obtain written permission from Springer-Verlag as well. However, Springer-Verlag may grant rights concerning journal issues as a whole.

To be signed by at least one of the authors who agrees to inform the others, if any.

_____
(Author's signature)

Please return your order form to:
Springer-Verlag Wien, Production Department, **Sachsenplatz 4-6, P.O. Box 89, A-1201 Wien, Austria**

Instruction to printer	Mark	Examples	
		In the text	In the margin
Character to be corrected		Letter to be corrected	e /
Group of characters to be corrected		Letters to be corrected	ed H
Several identical characters to be corrected		Council or Commission	o ///
Differentiation of several errors in the same paragraph		There are many faults in this lane	r/ m/ aF i L i
Character or word to be deleted		Commission and and Parliament	y y H
Character or word to be added		A word missing	is λ
Superior character required		The Court's judgment.	(1) /
Omitted text to be added (see copy)		1. January 12. December	Out see copy
Inferior character required		H_2SO_4	4 /
Change to italic		Ad infinitum	ital.
Change italic characters to roman		*status quo*	rom.
Change capitals to lower case		UNESCO	l.c.
Change to capitals or small capitals		Robert burns, AD 1759-96	Caps. S.C.
Change to bold face		This word needs emphasising!	bold
To be letter-spaced		These words need space	/
Correct horizontal alignment		This line is crooked	/
Text to be raised or lowered		This is a line uneven	/ /
Text to be aligned (to the left)		This text is to be aligned	/
Text to be aligned (to the right)		This text is to be aligned	/
Text to be centred		This text is to be centred	/
Take back to previous line		This hyph- en is unnecessary	/
Text to run on (no new paragraph)		... line. (No new paragraph here	/
Take forward to next line		This hy- hen is badly placed	/
Create new paragraph		... line. A new paragraph should begin here	/
Close up		A space is wrong here	/
Equalise space		This spacing is very uneven	/
Add space between words		A space is missing here	# /
Reduce space between words		These spaces are too big!	/
Add space between lines		These lines are too close together	#
Reduce space between lines		These lines are too far apart.	/
Stet (let original text stand)		This text was corrected error	✓
Transpose characters		These letters are transposed	/
Transpose words		These are words transposed	/
Transpose lines		transposed These lines are	/

NB: A correction made in the text must always have a corresponding mark in the margin, otherwise it may be overlooked when the corrections are made. The same marks should be used, where appropriate, by copy-editors marking up copy. Where instructional words are used in marginal marks, e.g. 'ital.', 'bold', etc., they must always be encircled to show that they are not to be printed.

Serie 6
01.03.VI

33,3 % cheaper for you ...

As a Springer-author you are now entitled to receive a 33,3 % price reduction on the list price of **all books** published by Springer Verlage Wien, Berlin/Heidelberg, New York, London, Paris, Barcelona, Tokyo and Hong Kong as well as Böhlau/Wien, Physica, Birkhäuser und Steinkopff. For your order please use this order form. Orders have to be sent directly to Springer-Verlag Wien.

Als Autor/in des Springer-Verlages erhalten Sie 33,3 % Rabatt auf den Ladenpreis der **gesamten Buchproduktion** der Springer-Verlage Wien, Berlin/Heidelberg, New York, London, Paris, Barcelona, Tokyo und Hong Kong sowie der angeschlossenen Verlage Böhlau/Wien, Physica, Birkhäuser und Steinkopff. Bitte bestellen Sie mit diesem Bestellschein. Ihre Bestellung senden Sie bitte ausschließlich an den Springer-Verlag Wien.

For detailed information about titles published by Springer-Verlag please visit our homepage.
Nähere Informationen über das Programm des Springer-Verlages finden Sie auf unserer Homepage.
http://www.springer.at

Order Form / Bestellschein

Springer-Verlag, Order Department, Sachsenplatz 4–6, P.O. Box 89, A-1201 Vienna, Fax +43.1.330 24 26
Springer-Verlag, Auslieferung, Sachsenplatz 4–6, Postfach 89, A-1201 Wien, Fax +43.1.330 24 26

I order herewith / Ich bestelle hiermit:

copy/ies	ISBN	Author	Title
Expl.	ISBN	Autor	Titel

Please copy this order form for your next orders. Bitte kopieren Sie diesen Bestellschein für Ihre weiteren Bestellungen.

o Please bill me / Bitte liefern Sie gegen Rechnung

o Please charge my credit card / Bitte belasten Sie meine Kreditkarte

o VISA o MASTERCARD o AMEX o DINERS

Card No. / Karten-Nr. ..... Expiry date / Gültig bis .....

NAME / NAME .....

ADDRESS / ADRESSE .....

.....

DATE / DATUM .....

SIGNATURE / UNTERSCHRIFT .....

SpringerGeosciences

Bernhard Hofmann-Wellenhof,
Herbert Lichtenegger,
James Collins

Global Positioning System

Theory and Practice

Fifth, revised edition.
2001. XXIII, 382 pages. 45 figures.
Softcover EUR 51,– (Recommended retail price)
Net-price subject to local VAT.
ISBN 3-211-83534-2

This new edition accommodates the most recent advances in GPS technology. Updated or new information has been included although the overall structure essentially conforms to the former editions. The textbook explains in comprehensive manner the concepts of GPS as well as the latest applications in surveying and navigation. Description of project planning, observation, and data processing is provided for novice GPS users. Special emphasis is put on the modernization of GPS covering the new signal structure and improvements in the space and the control segment. Furthermore, the augmentation of GPS by satellite-based and ground-based systems leading to future Global Navigation Satellite Systems (GNSS) is discussed.

Contents

Introduction • Overview of GPS • Reference systems • Satellite orbits • Satellite signal • Observables • Surveying with GPS • Mathematical models for positioning • Data processing • Transformation of GPS results • Software modules • Applications of GPS • Future of GPS • References • Subject index

"... Although developed as a classroom text, the book is also useful as a reference source for professional surveyors and other GPS users. This because it covers both GPS fundamentals and leadingedge developments, thus giving it a wide appeal that will clearly satisfy a broad range of GPS-philes ... The volume cogently presents the critical aspects and issues for users, along with the theory and details needed by students and developers alike. For those seriously entering the rapidly changing GPS field, this book is a good place to start." GPS WORLD

Yong-Qi Chen,
Yuk-Cheung Lee (eds.)

Geographical Data Acquisition

2001. XIV, 265 pages. 167 figures.
Softcover EUR 62,– (Recommended retail price)
Net-price subject to local VAT.
ISBN 3-211-83472-9

This book is dedicated to the theory and methodology of geographical data acquisition, providing comprehensive coverage ranging from the definition of georeferencing systems, transformation between these systems to the acquisition of geographical data using different methods. Emphasis is placed on conceptual aspects, and the book is written in a semi-technical style to enhance its readability. After reading this book, readers should have a rather good understanding of the nature of spatial data, the accuracy of spatial data, and the theory behind various data acquisition methodologies. This volume is a text book for GIS students in disciplines such as geography, environmental science, urban and town planning, natural resource management, computing and geomatics (surveying and mapping). Furthermore it is an essential reading for both GIS scientists and practitioners who need some background information on the technical aspects of geographical data acquisition.

Contents

Geographical Data and Its Acquisition (Yuk-Cheung Lee) • Coordinate Systems and Datum (Esmond Mok, Jason Chao) • Transformation of Coordinates between Cartesian Systems (Xiao-Li Ding) • Map Projections (Yuk-Cheung Lee) • Geographical Data from Analogue Maps (Yuk-Cheung Lee, Lilian Pun) • Ground-Based Positioning Techniques (Steve Y.W. Lam, Yong-Qi Chen) • Satellite-Based Positioning (Esmond Mok, Günther Retscher) • Techniques for Underwater Data Acquisition (Günther Retscher) • Image Acquisition (Bruce King, Kent Lam) • Orthoimage Generation and Measurement from Single Images (Zhilin Li) • Geometric Data from Images (Bruce King) • Thematic Information from Digital Images (Qiming Zhou) • Current Trends in Geographical Data Acquisition: An Epilogue (Zhilin Li, Yong-Qi Chen)

SpringerWienNewYork
Sachsenplatz 4-6, P.O. Box 89, A-1201 Wien • Fax +43-1-330 24 26, e-mail: books@springer.at, Internet: **www.springer.at**